UCLA
UCLA Electronic Theses and Dissertations

Title
Measurement of Drag Reduction on Parallel Trench Superhydrophobic Surfaces in a High-Speed Water Tunnel

Permalink
https://escholarship.org/uc/item/6n97c3sj

Author
Kerezyte, Gintare

Publication Date
2017

Peer reviewed|Thesis/dissertation

eScholarship.org Powered by the California Digital Library
University of California

UNIVERSITY OF CALIFORNIA

Los Angeles

Measurement of Drag Reduction on Parallel Trench Superhydrophobic Surfaces in a High-Speed Water Tunnel

A thesis submitted in partial satisfaction

of the requirements for the degree Master of Science

in Mechanical Engineering

by

Gintare Kerezyte

2017

© Copyright by

Gintare Kerezyte

2017

ABSTRACT OF THE THESIS

Measurement of Drag Reduction
on Parallel Trench Superhydrophobic Surfaces
in a High-Speed Water Tunnel

by

Gintare Kerezyte

Master of Science in Mechanical Engineering
University of California, Los Angeles, 2017
Professor Chang-Jin Kim, Chair

Superhydrophobic (SHPo) surfaces are capable of trapping air under water, and this air plastron may lubricate the shearing of the water flowing by and reduce its skin-friction drag. While the slip effect and the resulting drag reduction on SHPo surfaces have been well understood in laminar flows, the results have been controversial and inconsistent in regard to turbulent flows. This thesis describes the progressive modification and adaptation of a low-profile testing module that measures the relative drag of two surfaces for flow tests in a high-speed water tunnel. After a series of experiments at Naval Undersea Warfare Center (NUWC) in Newport, Rhode Island to improve the testing module until it functions reliably in their water tunnel, we obtain a functional prototype and complete successful measurements. Testing a set of SHPo surfaces in boundary layer flows

along the parallel trenches at Reynolds numbers up to $9.7x10^6$, we obtain drag reduction up to ~34% compared with a smooth surface. The results support previous numerical studies predicting that the rate of drag reduction increases with Reynolds number, visualize the wetting phenomena of SHPo surfaces in high-speed water tunnel tests, and lay the groundwork to study the effect of SHPo surface trench parameters.

The thesis of Gintare Kerezyte is approved.

Ajit K. Mal

Hossein Pirouz Kavehpour

Chang-Jin Kim, Committee Chair

University of California, Los Angeles

2017

This thesis is dedicated to my family and friends, for their love, support, patience, and belief in me and my future.

Table of Contents

List of Figures

List of Tables

Acknowledgements

I would like to first acknowledge my advisor Professor Chang-Jin "CJ" Kim for giving me this great opportunity to learn so much about fluid dynamics, machining, and running experiments and for teaching me to be a good presenter and a thorough, responsible researcher. I would also like to thank Professor Ajit Mal and Professor Pirouz Kavehpour for being on my thesis committee and for being patient, encouraging, and excellent teachers during my graduate studies.

I am grateful for all the members of the Micro and Nano Manufacturing Laboratory for making my past two years on the project fun and fulfilling. A huge thanks to Muchen Xu for being a patient, inspiring mentor and friend. Also, I really appreciated all the help and advice Benjamin Tan, Miguel Lozano, Jose Sanchez, and Anatoly Matus offered during my prototype manufacturing.

I would also like to sincerely thank the engineers at the Naval Undersea Warfare Center, especially to Charles Henoch, Dana Hrubes, Robert Kuklinski, Justin Rockwell, and Al Fredette. Thank you for helping me troubleshoot my software and hardware problems, creating a welcoming environment, and showing me how truly beautiful and friendly Rhode Island can be.

Last, but definitely not least, I am so grateful for all the love and encouragement my mom, dad, brother, and Gerrit Lane have given me. I am very lucky to call them family and my best friends who have provided me endless support for reaching my dreams and full potential.

The research described in this thesis was sponsored by the Defense Advanced Research Projects Agency (DARPA) (Award No: HR0011-15-2-0021) and approved for public release. The content of the thesis does not necessarily reflect the position or the policy of the government.

Chapter 1 Introduction

1.1 Objective

Using the fabrication technology of micro electro mechanical systems (MEMS), researchers have had great success manufacturing superhydrophobic (SHPo) surfaces and understanding how they induce a slip to the liquid flowing over them. One of the most economically and environmentally beneficial applications for these surfaces is underwater skin-friction drag reduction for moving vessels. While researchers have collected sufficient evidence of drag reduction on SHPo surfaces in laminar flows, phenomena and trends in turbulent flows have been controversial and not conclusive [1][2]. This is in part due to the challenge of measuring the drag accurately and confirming surface conditions in turbulent flow environments.

Researchers at the UCLA Micro and Nano Manufacturing Lab have developed a MEMS-based floating plate drag sensor, capable of directly measuring skin friction on two surfaces, for quantifying the relative drag, i.e., the drag force on one (e.g., SHPo) surface relative to that on the other (e.g., smooth) surface in turbulent flows [3]. Inspired by an earlier design of a silicon-based drag sensor, which mounted two 1cm by 2cm surface samples [4], Dr. Muchen Xu has developed a metal-based drag sensor that can test two 4cm by 7cm surface samples for his Ph.D. research. This thesis documents the process of adapting the metal drag sensor for use in a high-speed water tunnel environment and reports the results of multiple experiments leading to successful quantification and characterization of drag reduction on parallel-trench SHPo surfaces. This chapter begins with an introduction to the testing system and environment. Subsequent chapters describe in detail the design and success of three successive testing module prototypes.

1.2 Hardware

The shear stress sensor, developed by Dr. Muchen Xu for his Ph.D. research to measure drag reduction on SHPo surfaces and adapted in this thesis to be used in a water tunnel, is made up of mechanical and optical systems. The mechanical system flexurally suspends a floating plate that linearly displaces along the flow direction by an amount proportional to the local skin friction drag on the sample surface attached on the floating plate. The optical system detects the movement of a ruler on the back of the floating plate and records the changes in analog signal; then, the analog signal is converted to a digital reading of counts, proportional to the surface's metric displacement.

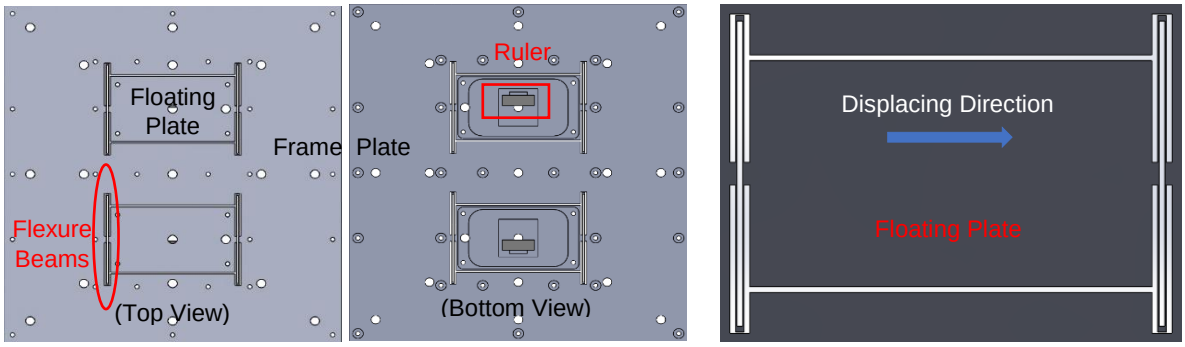

Figure 1.1: Mechanical system of the shear stress sensor (drag sensor), with two floating plates to mount two surface samples. (a) Top and bottom views of the frame plate with its components: floating plates, flexure beams, rulers. (b) Zoomed-in view of one floating plate, showing the flexure beam design.

The mechanical system is comprised of: a frame plate, floating plate(s), and a ruler (Figure 1.1). The frame plate is an aluminum piece meant to hold the floating plate(s) and is the main point of attachment to the testing module (Figure 1.1 (a)). The floating plate(s) is formed

when a set of flexure beams is cut into the frame plate by electrical discharge machining (EDM) (Figure 1.1 (b)). The layout of the flexure beams allows movement of the floating plate in one direction, which will be aligned to the flow direction. A large beam thickness-to-width ratio restricts the movement to longitudinal, preventing transverse, vertical, or rotation movement [1]. The geometry of the flexure beams is varied to create spring constants specific for displacement ranges predicted for various experiments. The displacement (*d*) is linearly proportional to skin friction drag experienced by the floating plate(s):

$$d = [\frac{l^3}{(24EI)}]F_s \tag{1.1}$$

where *l* is the length of the flexure beam, *E* is Young's modulus (69GPa for aluminum), F_s is the frictional force and *I* is the second moment of area for beam cross section ($I = \frac{tw^3}{12}$), where *t* is the thickness and *w* is the width of the beam [1]. For use in a water tunnel capable of flow speeds 2-9m/s, a drag range of 0.006-0.266N and a shear stress range of 2-95Pa on a sample surface of 4cm by 7cm were predicted. To determine the ideal spring constant for the floating plate in this environment, the force measurement resolution was divided by the optical measurement resolution. The force measurement resolution is 10% of the minimum force:

$$\mathrm{F} = (0.1)(\tau_{min})(\mathrm{A}) = (0.1)(2\mathrm{Pa})(70\mathrm{mm})(40\mathrm{mm}) = 560\mu\mathrm{N} \tag{1.2}$$

where *F* is the force measurement resolution, τ_{min} is the minimum shear stress, and *A* is the sample area. The optical measurement resolution is defined by the spacing between the micropatterned gratings (20μm) on the ruler. Thus, the desired spring constant of the floating plate system to be used in a water tunnel environment was calculated to be ~7100N/m; throughout the thesis project, multiple floating plate systems were used in the range of 6500-8500N/m [3]. The glass

ruler, sold by Celera Motion [5], is the last component of the mechanical system; it is attached to the back of, and moves with, the floating plate (Figure 1.1 (a)). The optical system tracks the ruler's gratings to quantify the movement.

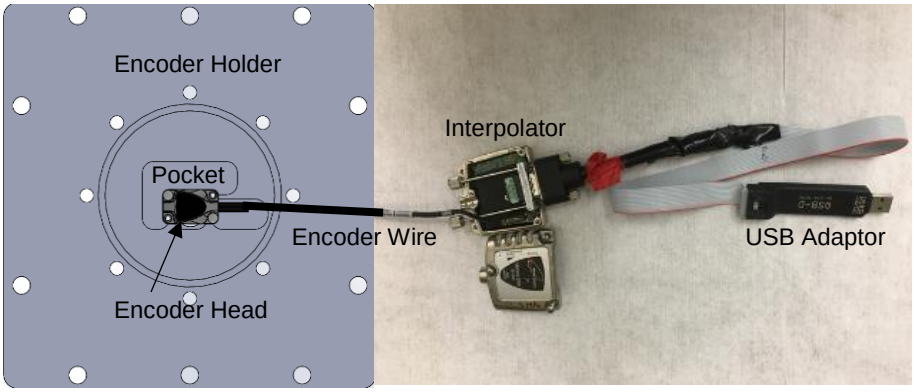

(a) (b)

Figure 1.2: Optical system of the shear stress sensor. (a) Bottom view of the encoder holder; the encoder head's laser is shining into the page. (b) Picture showing how the encoder is ultimately connected to the computer via USB adaptor.

The optical system is comprised of: encoder holder, encoder(s), interpolator(s), and USB adaptor(s) (Figure 1.2). The encoder holder is an aluminum piece that houses the encoder(s); it is designed to structurally enforce the alignment specifications for the encoder. For the second testing module prototype, the encoder holder is not its own piece, but rather built into the water tunnel window. The encoder, the Mercury 1000 model sold by Celera Motion, is an infrared laser diode, with a wavelength of 850nm (Figure 1.2 (a)) [6]. The encoder's laser points at the ruler and records changes of the reflected light's intensity seen when the ruler's gratings are displaced. In order for the encoder to successfully track the ruler's movements, the positions of the ruler and encoder lens must be within tolerance: $z \pm 0.15$mm, $y \pm 0.20$mm [6]. The encoder transmits the light intensity information to the interpolator, SmartPrecision Electronics Module sold by

Celera Motion [6], which converts it to an analog signal (Figure 1.2 (b)). The interpolator has four LED lights that flash different colors depending on if the system is on and aligned. Lastly, the interpolator is connected to a USB adaptor, QSB module sold by US Digital [7], that converts the analog signal to digital and reads it into the computer software as counts (1 count = 0.078microns) (Figure 1.2 (b)). The specifications and tolerances of the mechanical and optical systems were carefully incorporated into the design of window A discussed in Chapter 2.

1.3 Software

The software used to read in the displacement data is provided by US Digital upon purchase of the QSB module. The displacement data is displayed in real-time on a dial gauge (Figure 1.3 (a)). The dial gauge can move in the clockwise or counterclockwise direction depending on the position and displacement direction of the ruler. Considering the dial gauge can move in either direction, the *Cycles Per Revolution* parameter has to be set large enough to make sure that the displacement will never pass the half way point (2000 counts) on the dial gauge. If it passes the half way point, then you cannot be sure if the displacement was small (less than half) in the negative direction or large (greater than half) in the positive direction. Before the displacement data can be read and stored in a text file, *Samples to Collect*, *Output Interval Rate*, and *Log File* (save location) needs to be set (Figure 1.3 (b)). Depending on how long you want to collect data you can determine the *Samples to Collect* value:

$$S = 512t/R \tag{1.3}$$

where S is the *Samples to Collect* value, t is how long you want to collect data, R is the *Output Interval Rate* (if set as 1 the software will collect 512 samples/sec).

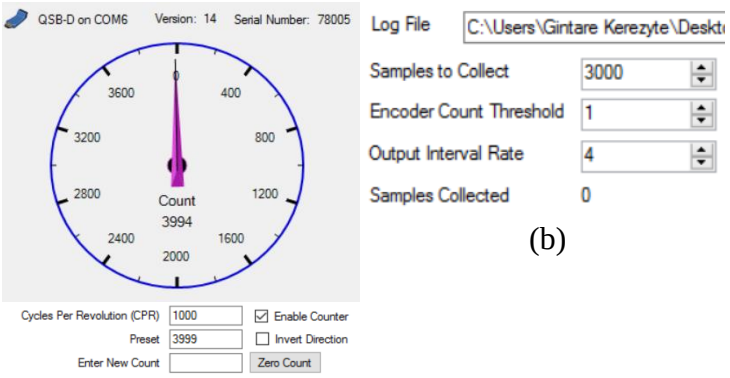

Figure 1.3: Software interface. (a) Dial gauge, *Cycles per Revolution* value marks ¼ of the dial. (b) Settings that can be manipulated to change experiment recording length.

After the data has been collected, the data is saved as a text file that can later be analyzed with excel. The data is manipulated in excel with an "if, else" statement so that we know the displacement direction. For example, if the cycles per revolution is set to be 1000, then the "if, else" statement reads: if # > 2000, # - 4000, else #. Therefore, a displacement reading of 3800 is converted to -200counts, meaning the ruler was displaced in the negative direction. Ultimately, displacement data is plotted over time at various speeds and for various surfaces.

1.4 Surface Samples

The shear stress sensor is used to measure the skin friction coefficient felt by various types of SHPo surfaces in turbulent flow conditions. In order to quantify the drag reduction on SHPo surfaces relative to a smooth surface, data for a control (i.e., smooth) surface also needs to be collected. All the samples are fabricated in a cleanroom from a silicon wafer, cut into rectangular shapes (40mm x 70mm) using a dicing saw, and coated with hydrophobic Teflon. The difference between the control and SHPo samples is how they are processed from the silicon wafer. The

control sample has had nothing done to it and thus remains smooth; in future discussions, this sample is referred to as the Smooth sample. The SHPo samples are lithographically etched and thus have microscopic trenches arranged in parallel. The gas fraction of the SHPo sample can be adjusted by varying the trench dimensions:

$$GF = (P - W)/P \tag{1.4}$$

where GF is gas fraction, P is pitch of grates, and W is width of grates [1] (Figure 1.4).

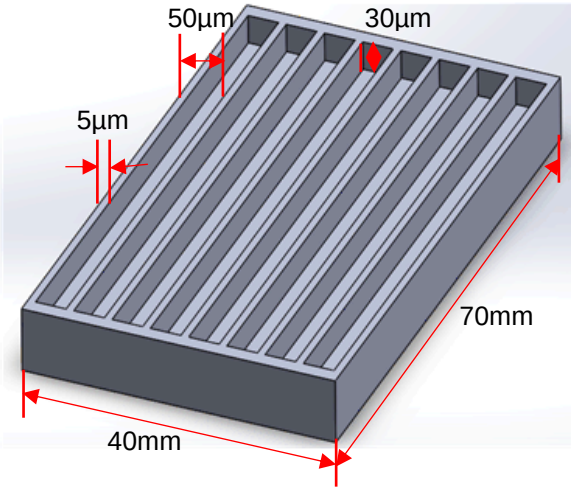

Figure 1.4: Geometric parameters of sample surface. Example of a SHPo sample with pitch = 50µm, width of grates = 5µm, height of grates = 30 µm. Gas fraction would be (50-5)/50 = 0.9 (90%).

Past research with laminar flows has proven the trend that increasing gas fraction increases slip length and drag reduction rate [1] [8], and we anticipate the increased slip length will increase the drag reduction in turbulent flows as well. Drag reduction data will be collected for various types of SHPo samples to prove this trend holds in turbulent conditions.

1.5 Water Tunnel

All the experiments for this thesis were run in a water tunnel at the Naval Undersea Warfare Center (NUWC) in Newport, Rhode Island. This water tunnel was chosen for its high Reynolds number capabilities and their technical and administrative support under the project funded by DARPA. The test section of the water tunnel is square in cross section and 10ft long and made of four interconnected rectangular sections (Figure 1.5). Any of the four windows of the four sections can be removed and replaced with a testing module window. The testing module window panel was fabricated to exactly match the standard window panel design to ensure installation compatibility, avoid leaks, and preserve a uniformly flat inside surface of the water tunnel. Design modifications were made to the center region of the testing module window panel to accommodate the shear stress sensor, as discussed in Chapter 2.

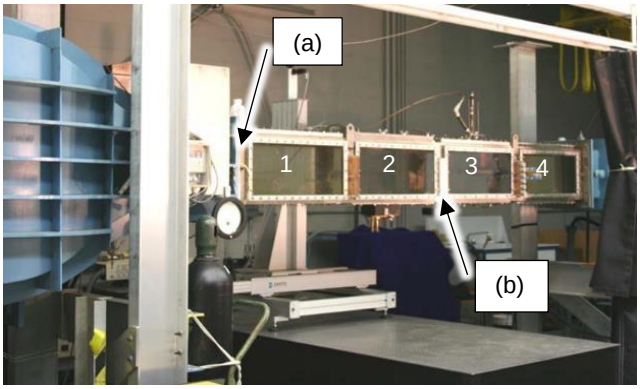

Figure 1.5: NUWC water tunnel. Testing section is made up of four window sections labeled #1-4. (a) Inlet distance reference. (b) Water tunnel cage holding all the windows.

The testing module window was installed in place of standard bottom window in position 2 or 3 of the water tunnel. The bottom position was chosen so that the testing module window would hold the sample surfaces right-side up, avoiding any interaction with air bubbles floating

along the top of the water tunnel. These air bubbles were introduced into the water tunnel at high speeds due to imperfections of the tunnel's structural sealing, and could have directly affected displacement data if the surfaces were upside-down.

The testing module window holds the surface samples flush with the inner surface of the water tunnel so that the turbulent boundary layer is not disrupted; the preserved boundary layer length can be measured from the start of the water tunnel (Figure 1.5 (a)) to the center of the sample. However, this distance is only an estimate, because the start of the boundary layer development was not precisely known. Also, the cage of the water tunnel (Figure 1.5 (b)) was found to be lower than the windows it holds; the height different was as much as 0.02in and was not uniform left to right. It is not clear whether these steps disrupted the boundary layer significantly enough to change the inlet distance value used in calculating theoretical skin friction coefficient (C_f) on a smooth surface:

$$C_{f,theoretical} = (2\log(Re_x) - 0.65)^{-2.3} \tag{1.5}$$

where $Re_x = \frac{uL}{\upsilon}$, u = velocity of fluid (m/s), L = distance of sample center to inlet (m), υ = kinematic viscosity of water at room temperature = $1\text{x}10^6$ m^2/s. Similarly, theoretical shear stress (τ) on a smooth surface is calculated:

$$\tau_{theoretical} = (C_{f,theoretical})(\frac{\rho u^2}{2}) \tag{1.6}$$

where ρ = density of water = $1000kg/m^3$.

These values were calculated for various speeds and compared to experimental smooth data as one way of checking the success of the testing module design. Note that even if the theoretical and experimental Smooth surface data do not match, potentially due to the imprecise

inlet distance estimation or a disruption of the boundary layer, the experimental Smooth surface data can still be compared against the experimental SHPo surface data to determine relative drag reduction. This robustness is indeed one of the key features of the relative shear sensor used for this research.

The water tunnel was operated by inputting desired speed in terms of revolutions per minute (RPM) and waiting 1-2 minutes for the water to stabilize at that speed. The water tunnel can reach speeds up to 675RPM (9.5m/s). The NUWC engineers provided data relating RPM values to speed (m/s) values measured with a pitot tube (Table 1.1).

Table 1.1: Water tunnel RPM settings corresponding to speed values in the NUWC water tunnel. Courtesy of Charles Henoch and Dana Hrubes.

RPM	Speed (m/s)
75	0.95
152	2.05
228	3.15
300	4.15
375	5.25
450	6.4
525	7.5
600	8.5
675	9.5

Chapter 2 Testing Module Prototype A and Flow Experiments

2.1 Design Parameters

The two most fundamental design characteristics of testing module window panel A were that it had to fit inside the water tunnel and had to hold the shear stress sensor. The first characteristic was satisfied by copying the traditional water tunnel window design, provided by the NUWC engineers. The most important water tunnel fit compatibility parameters were the (1) depth and shape of the outside ledge and (2) spacing of the holes around the perimeter of the window to allow for tight and secure attachment to the water tunnel (Figure 2.1 (b)). The second fundamental characteristic was satisfied by designing central pockets (1) big enough to house the entire shear stress sensor, (2) with enough room for adjustment to ensure all the components are flush with the bottom of the water tunnel, and (3) with an exit hole for the encoder wire to connect to the computer outside of the water tunnel (Figure 2.1 (b)).

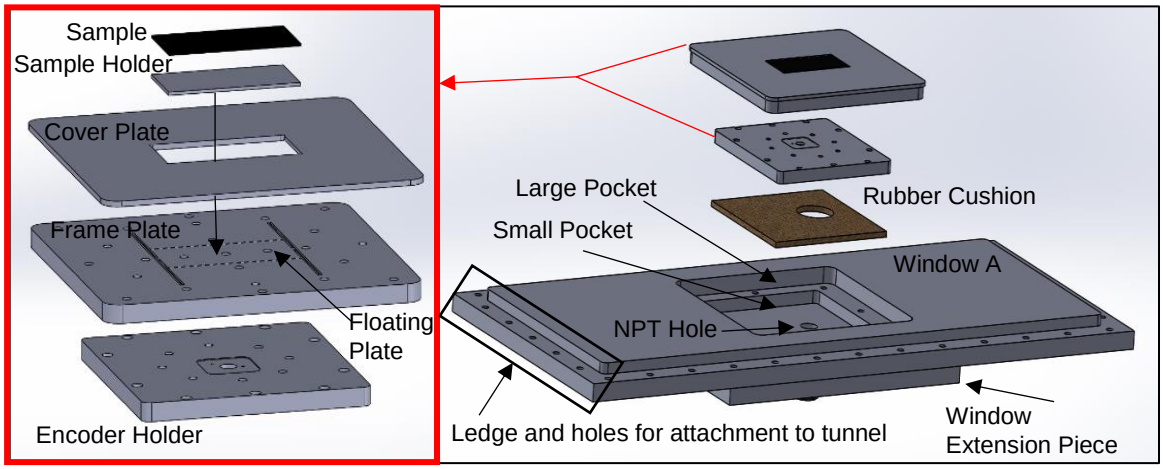

(a) (b)

Figure 2.1: Window panel A shown in 3D CAD layout. (a) Exploded view of the shear stress sensor and its accessory components. (b) Exploded view of the window panel assembly; emphasizing the structural design of window panel A.

The shear stress sensor described in Chapter 1 requires the design and incorporation of two accessory components to prepare for use in the water tunnel. The complete sensor thickness, including the accessory components, determines the necessary depth of the pockets in window A. The first accessory component is a sample holder, a thin acrylic rectangular block meant to hold the thin fragile sample surface (Smooth or SHPo). Each sample to be tested is securely taped, with strong, water-insoluble tape, onto its personal sample holder. The sample holder is then taped to the center platform of the floating plate, making sure not to obstruct the beams (Figure 2.1 (a)). The second accessory component is a cover plate meant to cover the frame plate and create a uniform top surface exposed to the water flow. The cover plate is designed to be thick enough to align with the top of the sample being tested and to cover any exposed screw holes and beams on the frame plate (Figure 2.1 (a)). The cover plate should be a uniform slab of material, chosen to be acrylic to minimize the weight of the system, with a rectangular hole cut

out in the center for the sample; the rectangle's length is bigger than the sample's to allow room for the sample to displace in the flow direction. Also, two shallow pockets in the shape of the floating plate's beams are necessary to preserve the free movement ability of the floating plate's center platform (Figure 2.2). Threaded blind holes on the cover plate must align with the clearance holes on the frame plate to hold the two surfaces together from the back (Figure 2.2).

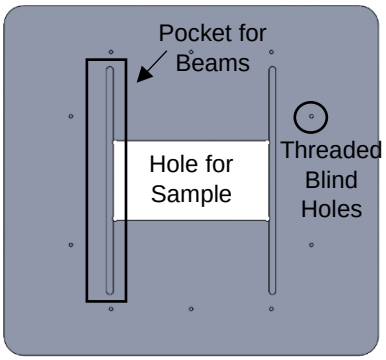

Figure 2.2: Back view of the cover plate.

The mechanical and optical systems of the shear stress sensor used in window A were borrowed from an old test setup and needed to be adapted for the new one. Based on the previous design, as long as the frame plate and encoder holder are held firmly up against each another, the encoder's specifications, provided by Celera Motion [6], are preserved (Figure 2.3). For the old setup, the frame plate's inner threaded holes were used for attachment to the encoder holder, securing the proper x and y alignment of the ruler and encoder lens. However, for the new setup, these inner threaded holes are modified with Heli-coil inserts for cover plate attachment instead; none of the frame plate's inner threaded holes are available for encoder holder attachment and so the x and y alignment must be structurally enforced by the window pocket's design instead. The last and most crucial adaptation was preparing the encoder holder, previously only used in air, to

be used in water. The encoder holder was waterproofed with a layer of Teflon tape and silicone sealant at the wire exit.

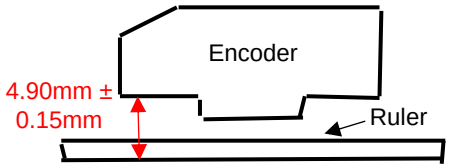

Figure 2.3: Schematic of Celera Motion's specification for z-axis alignment of encoder and ruler.

The design of window A incorporates two pockets. Both pockets' x and y dimensions are designed 0.5mm bigger than parts they hold, to account for machining error and allow room for alignment adjustment. The large pocket holds the mechanical system of the shear sensor. Through-holes around the perimeter of the pocket, aligning with the frame plate's outer threaded holes, must be incorporated as a means of attaching the mechanical system to the window. The large pocket's depth is 0.5mm deeper than the thickness of the assembled frame plate and cover plate to compensate for machining error and allow room for spacers to make the cover plate and window flush (Figure 2.1 (b)). It is better to make features deeper or thinner, instead of accidentally too shallow or thick, because it is easier to add spacers than shave off material. Room for spacers is also a necessary consideration for the design of the sample holders to help make the sample and window flush. Ensuring flushness of the cover plate, sample, and inner window surface within 0.02mm is very important for preventing disruptions in the boundary layer flow and preserving the accuracy of drag reduction measurements [9]. The second pocket is inside the large pocket and holds the optical system of the shear sensor (Figure 2.1 (b)). This pocket's depth is 5mm deeper than the thickness of the encoder holder to allow room for a piece of rubber. This piece of rubber, thicker than 5mm, will be compressed 15% when the mechanical

system is screwed into its pocket, pushing the encoder holder up against the bottom surface of the frame plate (Figure 2.1 (b)).

The design of window A also incorporates a National Pipe Thread (NPT) threaded hole (Figure 2.1 (b)) to provide a way for the optical system of the shear stress sensor to connect to a computer outside of the tunnel. Considering the optical system is submerged in water during the experiment, the encoder wire is run through a liquid-tight cord grip, screwed into the window NPT hole, to prevent excessive water leakage. In order to have a reasonable number of threads along the hole and enough material reinforcing the bottom of the deepest pocket, a supporting acrylic piece is acrylic bonded onto the main window (Figure 2.1 (b)). The extension piece is designed to not interfere with the window's attachment to the water tunnel, to avoid any complications of accommodating a thicker than standard window.

2.2 Experimental Procedure

The cover plate, frame plate, and floating plate unit are transported to the NUWC facility preassembled. Only the sample holder with the sample surface has to be attached on site. Once it is attached, the sample's flushness with the cover plate has to be verified under a microscope. If the sample is not within 0.02mm of the cover plate height, the spacers underneath the sample holder have to be readjusted. The spacers are customized by layering various thicknesses of tape depending on the leverage necessary (Figure 2.4). The encoder holder and encoder sensor are also transported pre-assembled, while the interpolator and USB connector are attached after the encoder wire is threaded through the liquid-tight cord grip on the window.

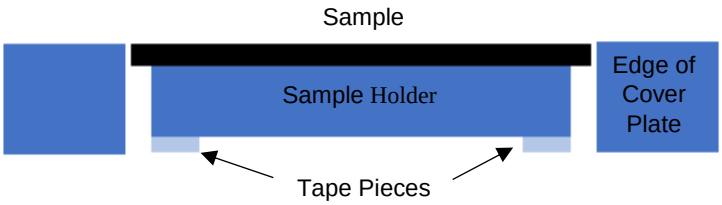

Figure 2.4: Schematic of sample flushness. Spacers are introduced under the sample holder to push the sample up to become flush with the surrounding cover plate.

The bottom window of the water tunnel test section #2 is removed and replaced with our testing module window panel A. The top window of the water tunnel test section #2 is also removed to allow access for system installation. The encoder wire is run through the liquid-tight cord grip and the encoder holder is placed in the center of the second pocket on top of the rubber piece. The through-holes around the perimeter of the large pocket are temporarily sealed with rubber stoppers while the water tunnel is filled to 70%, high enough to assemble the system underwater (Figure 2.5).

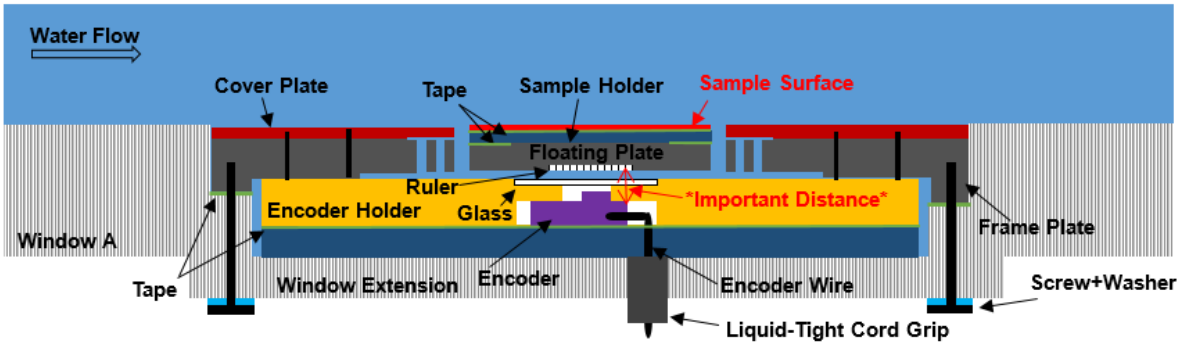

Figure 2.5: Cross-sectional schematic of window panel A.

The completely assembled mechanical system is submerged inside the water tunnel and a pipette, filled with water, is used to push away any bubbles stuck on the back of the floating plate, between the floating plate beams, and along or on the sample. Bubbles are cleared from

the test section to prevent them from blocking the encoder's view of the ruler or interfering with the beam's displacement. The mechanical system can then be placed inside the large pocket. As the rubber plugs are one-by-one replaced by screws, the mechanical system is pulled down against the encoder holder. After the screws are tightened the flushness between the cover plate and window is checked by touch with fingers (Figure 2.5). If it is not flush enough, the screw tightness or spacer thickness beneath the frame plate are adjusted. The rest of the optical system of the shear stress sensor must be assembled and plugged into the computer to check the interpolator LED lights for alignment verification. If the lights are green, the system is ready to go, and if they are red, the mechanical system must be loosened and realigned.

Once the shear stress sensor is successfully installed and aligned, the top window is reattached, and the water tunnel is filled to the top. The water tunnel must be run at a low speed to clear the bubbles at the top of the tunnel before the experiment can commence. The USD Device Explorer software is setup with 1000 cycles per revolution, the "Samples to Collect" value is changed according to how long the data needs to be collected, and the software is zeroed at static water tunnel conditions. The data collection periods can vary from two to five minutes depending on the speed; higher speeds reach stabilization faster than lower speeds.

The data collection period starts at static conditions, includes the increase up to target speed, stabilization at target speed, and decrease back to zero flow, and ends back at static conditions. The average displacement value at static conditions is subtracted from the average displacement value at target speed to determine the absolute displacement recorded at that speed. This process is repeated for multiple speeds for the Smooth sample and compared against the theoretical displacement values predicted by Equations 1.5 and 1.6. The accuracy of the testing module and shear stress sensor is not only determined by comparing the experimental displacement values to

theoretical, but also by checking that the displacements at the start and end of each collection period are similar and close to zero.

2.3 Trip #1 Experiments and Results

During Trip #1 (1-day experiment), only data for 152RPM (2m/s) was successfully collected before the interpolator LED light started blinking red, signaling a problem. The top window was removed and the sensor was de-attached to determine the problem. Water was found inside the encoder holder, proving the Teflon and silicone sealing to be insufficient means of waterproofing. Once the encoder is wet, it stops functioning until dried overnight; this was a one day trip, so no more data could be collected.

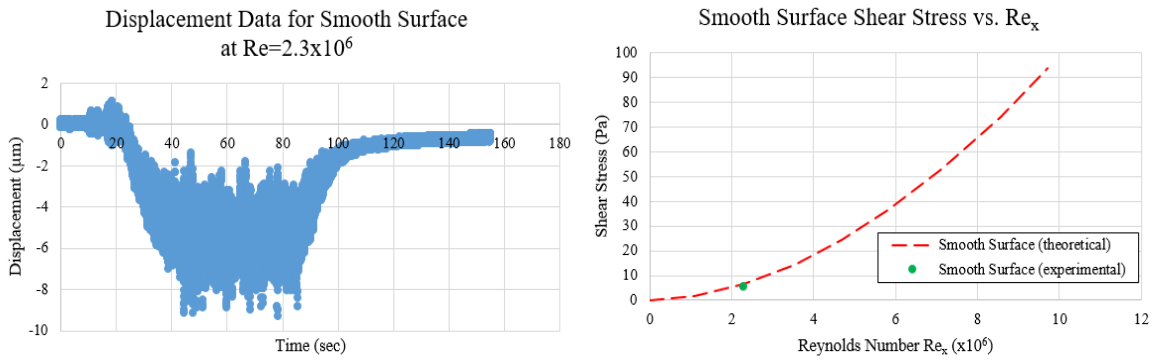

(a) (b)

Figure 2.6: Data from Trip #1. (a) Graph plotting displacement of a smooth surface against time. (b) Graph comparing experimental vs. theoretical shear stress data for a smooth surface at Re = $2.3x10^6$.

The data plot collected for displacement of a smooth surface at 2m/s followed a predicted pattern; displacement increase from zero (in the negative direction), stabilized at a value, and

then decreased back to zero (Image 2.6 (a)). The absolute displacement at 2m/s was recorded to be 5.36 microns, which can be used to calculate skin friction coefficient (C_f) and shear stress (τ):

$$C_{f,experimental} = (\frac{2}{\rho u^2})(\frac{xk}{A}) \quad (2.1)$$

$$\tau_{experimental} = (C_{f,experimental})(\frac{\rho u^2}{2}) \quad (2.2)$$

where ρ = density of water = 100kg/m^3, u = velocity of water = 2m/s, x = displacement of sample = 5.36µm, k = spring constant of floating plate = 3500N/m, A = area of sample = 3200mm^2.

The experimental shear stress value was calculated to be 5.80Pa and then compared to the theoretical shear stress of 6.51Pa (Equation 1.6), revealing an 11% error in the sensor measurement (Figure 2.6 (b)). This error could be due to the encoder malfunctioning due to water leakage; it could also be influenced by the inaccuracy of the inlet distance value, used in the theoretical shear stress calculations, which is measured from an arbitrary start of the water tunnel to the center of the test window (1.143m) (Figure 1.5 (a)). Further analysis of the displacement plot shows that the average displacement values for the start and end of the test did not match. The tail end of the plot did not seem to stabilize by the end of the data collection period; there is a chance that, if given more time, the tail end may have reached the same displacement value as the front end of the plot. No particular conclusion can be made about the efficacy of the shear stress sensor and testing module window A, because of many external variables and lack of data points.

The biggest issue during Trip #1 was the poor waterproofing of the encoder holder. To avoid this situation again, the next testing module window B will house the encoder on the outside of the window, exposed only to air instead of water.

Chapter 3 Testing Module Prototype B and Flow Experiments

3.1 Design Parameters

Testing module window panel B will house a completely new shear stress sensor. The new frame plate now holds two floating plates to allow for simultaneous data collection from two different sample surfaces, one Smooth and one SHPo, during one flow test. Since the two should experience identical flow conditions when placed at the center point in a symmetric water tunnel, the difference in the shear forces experienced should solely be due to differences in skin friction drag. Unlike the two floating plates made by the photolithographic etching [3], the two made by wire EDM in the current shear sensor cannot be expected to be identical, requiring us to measure their spring constants after fabrication and compensate for the difference. While the absolute value of drag may be affected by many external uncertainties (e.g., flow conditions), the relative drag on the two floating plates is expected to be accurate because the uncertainties experienced by the two are the same and cancel out. Meanwhile, the optical system of the new shear stress sensor also has a design change; specifically, it excludes the encoder holder. The encoder head is now attached to a pocket in the back of the testing module window B instead. The shape of the pocket holding the encoder mimics the design of the old encoder holder (Figure 3.1 (a)); this pocket shape controls the x and y-axis alignment of the encoder lens with the ruler.

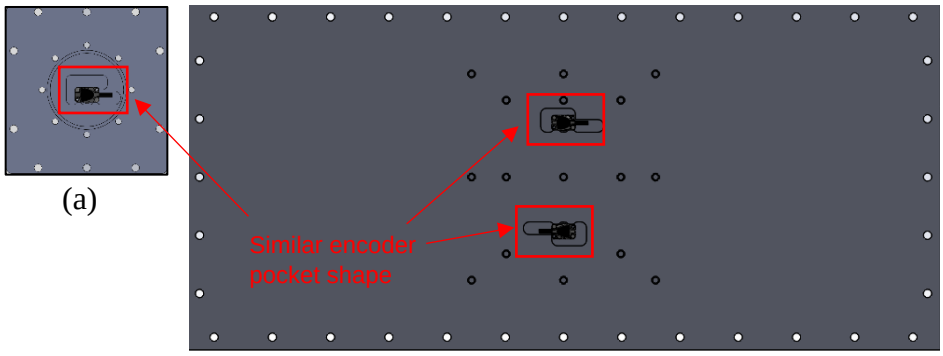

(a)

(b)

Figure 3.1: Diagram comparing encoder attachment between window A of Trip #1 and window B of Trip #2. (a) Backside view of the encoder holder from Trip #1, showing an encoder in a pocket. Window A is not shown as it has no provision to house the encoder. (b) Backside view of window B from Trip #2. Two encoder pockets are formed into window B to house two encoders.

Another big design change was made to the sample holders and how they attached to the center platforms of the floating plates. In the previous design (Chapter 2) schematically described in Figure 2.4, a sample was taped directly onto a sample holder, which was taped directly onto the floating plate. Once tape is used to attach the components, it is really difficult and time consuming to remove them. To make the process of replacing samples reasonably quick and convenient, the use of tape was limited. For the new design in this chapter for window B, threaded blind holes on the new sample holders match up with the clearance through holes on the new floating plates, so that the two surfaces can be screwed together from the back, instead of taped together. Next, the samples are too fragile and thin to incorporate screw holes, so instead screws are glued to the samples for attachment to the holders. The screws match up with holes in the sample holder, and are tightened onto the sample holder with nuts on the opposite side (Figure 3.2). This method uses no tape, and the same sample holder can be re-used for many samples. However, during Trip #2, it was discovered that screwing the samples onto the holders

caused them to bend and affect the drag data. To ensure that the sample remains completely flat, the old method of taping the sample, instead of screwing it, onto the sample holder was revisited for subsequent trips.

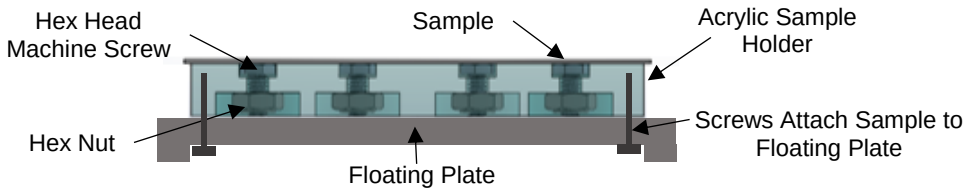

Figure 3.2: Schematic of the "glue screw" method of attaching a sample to a re-usable sample holder.

The design of window B incorporates two pockets on the inner surface of the window as shown in Figure 3.3. A cover plate and two sample holders are attached to the frame plate and the entire unit (mechanical system in Figure 3.3) must be housed in the main pocket of window B. To avoid direct contact of the floating plate beams with the bottom surface of the window pocket, which would prevent free displacement of the center platforms, another shallow pocket is introduced, as shown in Figures 3.3 and 3.4. Thus, the edges of the frame plate hold the middle suspended above the shallow pocket. Just like in the window A design, both pockets' x and y dimensions are designed 0.5mm bigger than parts they hold and the large pocket's depth is 0.5mm deeper than the thickness of the assembled frame plate and cover plate, leaving room for adjustment in all directions.

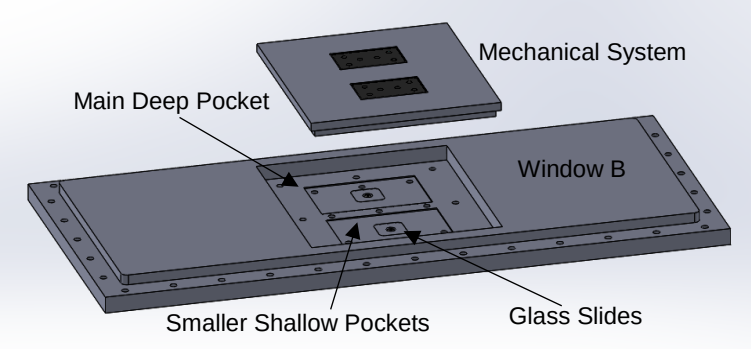

Figure 3.3: Window B 3D CAD layout. The mechanical system of the shear stress sensor is placed inside the window, while the optical system is attached to the outside (backside).

Next, the design of window B also incorporates two pockets on the outer surface of the window. These pockets are meant to house the two encoders (Figure 3.1 (b)). Unlike the pockets on the inner window B surface, the encoder pockets have very tight fitting designs. One corner of each pocket is used to fix the location of the encoders; many other features of window B rely on the encoder locations for reference. The depths of the encoder pockets must also be precise because spacers are difficult to use under the encoder and should be avoided. The depths of the encoder pockets are decided after the inside surface of the window is machined, because the resultant distance between the two pockets is directly related the z-direction distance specification for encoder installation (Figure 2.3). Ensuring that the distance between the encoder lens and bottom of the ruler is within the tolerance specified by Celera Motion [6] poses a big machining challenge, details discussed in section 3.2.

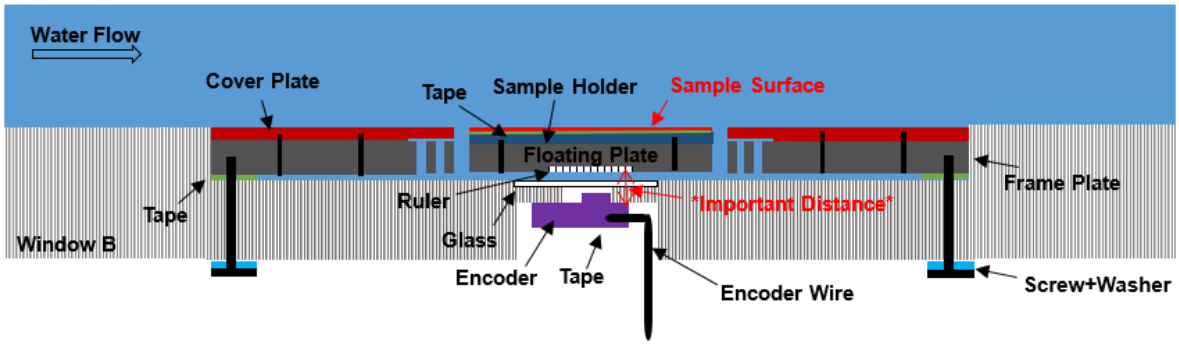

Figure 3.4: Cross-sectional schematic of window panel B.

Lastly, the design of window B requires two through clearance holes. The hole locations are strictly dependent on the dimensions of the encoder pockets; the holes allow the encoders to lay flat in the pocket, while the lenses stick out through the holes (Figure 3.3 and 3.4). These holes are covered with thin glass slides on the inside surface of the shallow pockets. Uniform adhesion of these glass slides is important to prevent water from leaking out when window B is installed and the water tunnel is filled with water. Since the encoders are attached to the outside surface of the window, a leak can be easily spotted and the encoder can be quickly removed and dried (Figure 3.5). This design is much more convenient than window A, where the encoder would sit in a puddle of water until the tunnel is drained and the frame plate is removed from the tunnel.

Figure 3.5: Picture of the bottom of window B. Encoders are screwed to the window (clear acrylic) and the lasers are pointing at the rulers on the back of the frame plate (silver aluminum).

3.2 Machining Challenges

The biggest challenge was machining the encoder pockets deep enough so that the encoder lens is 4.90mm ± 0.15mm away from the ruler (Figure 2.3), which is attached on a frame plate in a pocket on the opposite side of the window. Using a CNC, the top left corner of the inside surface of the window slab was indicated and the two pockets were milled. When the window was flipped over, the top right corner, was indicated to preserve the x and y-direction references and decrease machining error. Two through-clearance holes were then milled. A Mitutoyo depth micrometer was placed inside a clearance hole and used to measure the exact distance from the back of the window to a table surface flush with the top of the window. This provided an exact measurement of local window thickness, which cannot otherwise be measured. Knowing the thickness at each hole location, the encoder pocket holder depth was calculated. The top surface near each hole location was indicated separately so that the depth of each encoder pocket could be machined specifically. By measuring crucial dimensions throughout the machining process, machining errors could be minimized.

Another machining challenge was creating sample holders that were of a precise and uniform thickness. In order to hold samples perfectly flush with the surrounding cover plate, the sample holders must be an exact thickness:

$$t_{SH} = t_{CP} - t_S - t_T \tag{3.1}$$

where t = thickness, SH = sample holder, CP = cover plate, S = sample, T = tape between sample and sample holder. If the sample holders are machined one at a time, they can be clamped into a vise. Using a vise to clamp such a small and thin acrylic piece results in bending and warping; then, subsequent milling of a bent piece will result in a finished product with nonuniform thickness. An alternative option for sample holder manufacturing is mass production from one large piece of acrylic, taped to the CNC table. The non-uniformity of tape creates the same final product thickness problem seen after vise clamping a single piece. Thus, machining a sample holder with a 0.02mm thickness tolerance was found to be unreasonable. As a result, the sample holders were machined specifically less than the target thickness. When the sample holders were assembled in the shear stress sensor system, they were lower than the cover plate; different thicknesses of tape pieces were adhered to the bottom of the sample holder to raise them a desired height (Figure 2.4).

3.3 Experimental Procedure

For the experimental procedure, Trip #2 is very similar to Trip #1, except that now the encoders are not placed inside the water tunnel, but rather screwed to the outside of the window during window installation. Window B is placed in position #2 of the water tunnel testing area, like Trip #1. The same shear stress sensor assembly and water tunnel filling procedure is followed. The samples, sample holders, and floating plates are screwed together and the flushness with the surrounding cover plate is measured and adjusted.

Once everything is assembled, both encoders are connected to the computer via USB Adaptors so that displacement data for the Smooth and SHPo surfaces can be collected simultaneously. The experiment time is estimated to be about 125sec to ramp up to speed, 50sec at speed, and 125sec to ramp back down to zero speed, for a total of 300sec and thus 153600 samples to be collected (Equation 1.3). The experiment time is estimated from the Velocity versus Time graphs the NUWC engineers provided for each RPM level; based on their data, the water tunnel took the longest time, 125sec, to reach and stabilize at the lowest speed 75RPM (Table 3.1).

Table 3.1: Length of time needed for water tunnel to reach certain RPM.

RPM	Time (s)
75	125
152	90
228	80
300	65
375	70
450	75
525	85
600	90
675	100

When both encoders were prompted to record at the same time, a very long lag in data collection rate was seen. Instead of recording data from both encoders simultaneously, the software was found collecting them consecutively. It was collecting the entire data set of encoder #1 before encoder #2, resulting in an incomplete data set for encoder #2. The source of the problem could not be detected, even after checking software and computer parameters. The only change that eliminated the lag was using only one encoder at a time. Since this problem was found to be an inherent limitation of the encoder, we recorded the data for each encoder

separately in the following way. Displacement data was collected for encoder #1 for about a minute at static water tunnel conditions to record the baseline reference. Then, the tunnel was ramped up to Re = $1.09x10^6$, given enough time to stabilize at that speed, and data was collected for encoder #1 for about a minute. Next, the tunnel was ramped up to the next speed Re = $2.29x10^6$, given enough time to stabilize at that speed, and data was collected for encoder #1 for about a minute. This procedure of increasing speed and collecting data was repeated for Re = $3.54x10^6$, $4.69x10^6$, $5.83x10^6$, $7.14x10^6$, $8.57x10^6$, $9.72x10^6$. After data was collected for Re = $9.72x10^6$, the water tunnel was turned off, given enough time to stabilize at zero speed, and then the last data set was recorded for encoder #1 for about a minute. After ten data sets for encoder #1 (encoder beneath the smooth sample) the same procedure was repeated to record ten data sets for encoder #2 (encoder beneath the SHPo sample) during this two-day trip.

3.4 Trip #2 Experiments and Results

The displacement plots and values for Smooth and SHPo (Si (P50G90H50)) surfaces at each speed were checked for irregularities. The Smooth experimental displacement values were unreliable past Re = $5.83x10^6$, when the displacement versus time graphs showed signs of hitting a wall (Figures 3.6 (b) and 3.7). Also, the SHPo experimental data set became invalid past Re = $4.69x10^6$, when the data suddenly decreased instead of steadily increasing as predicted (Figure 3.7). This shift could have been due to the sample surface loosening from the sample holder, and thus any data taken after this physical change was no longer consistent with previous data and could not be reliably compared. During the experiment the Interpolator's LED light changed from green to red, meaning that some change during the experiment interrupted the sensor enough to warn for misalignment.

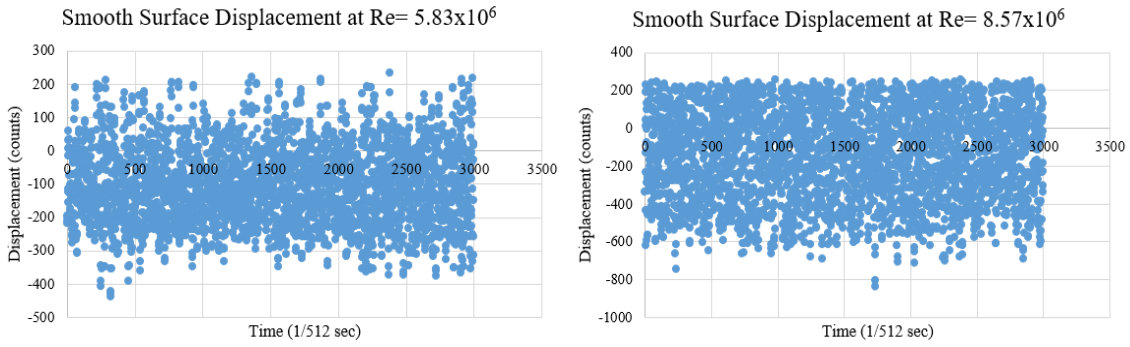

(a) (b)

Figure 3.6: Displacement versus Time plots for Trip #2. (a) Normal data trend for Smooth surface at Re = 5.83×10^6. (b) Abnormal data trends (signs of hitting a wall) for Smooth data at Re = 8.57×10^6.

The average displacement at each speed was determined and used to calculate the shear stress experienced on the sample. The Smooth experimental shear stress values, SHPo experimental shear stress values, and Smooth theoretical shear stress values were plotted against Reynolds number in Figure 3.7. It was expected that the shear stress values for Re = 0 at the beginning and end of the test should be the same. However, the start and finish values at Re = 0 were significantly different for both the Smooth and SHPo experimental data (Figure 3.7). A change of this magnitude is hypothesized to be caused by a physical shift of the sample or floating plate at high speeds.

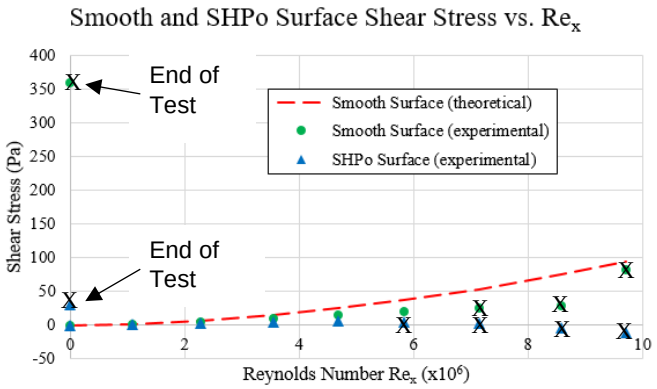

Figure 3.7: Shear stress versus Reynolds number plot for Trip #2. The X marks the unreliable data points due to physical hits or shifts. End of the test shear stress values did not return to zero.

Next, it was expected that the Smooth experimental shear stress data would match the Smooth theoretical data, but it was significantly less. The Smooth experimental displacement data showed signs of hitting a wall after Re = 5.83×10^6 (Figure 3.6 (b)), and so the last three data points were invalid and could not be used to compare to theoretical (Figure 3.7). Thus, it is not entirely clear how much the smooth experimental shear stress data differs from the theoretical and whether it is of great concern. Nonetheless, this difference could have been due to the Smooth sample not being perfectly flush with the cover plate; if the sample was a little under the cover plate, the shear stress it experienced would have been lower than usual. The lower than expected Smooth experimental shear stress values could have also been due to the imprecise value of inlet distance. Lastly, based on the idea that a SHPo surface experiences less shear stress than a Smooth surface due to the air retained in the microstructured grates, it was predicted that the SHPo experimental shear stress data would be lower than the Smooth at all speeds (Figure 3.7). This was found to be true, yet drag reduction comparisons for the two surfaces were not

done, because the data sets for Smooth and SHPo surfaces were collected consecutively not simultaneously.

Overall, the strange data trends from Trip #2 revealed areas of improvement, such as better methods of securing the samples from moving. Also, water tunnel speed should be allowed to ramp back down to zero between each speed data set, instead of only at the end of the experiment. By comparing beginning and end displacement values at Re = 0 for each speed, problems can be identified quicker. Lastly, the true reason for the data shifts is still unknown, whether it is a structural design error or something due to the water tunnel environment. Window B and the shear stress sensor must be further investigated after Trip #2 in a test tank back at the UCLA lab.

While collecting encoder displacement data for the two samples, pictures were taken of the sample surfaces to track any physical changes (Figure 3.8). As expected, the smooth surface showed no changes, because the surface has no air layer. On the other hand, the SHPo surface changed, became more or less wetted, with increasing flow speed. Typically, the SHPo surface is completely reflective, due to the trapped air (plastron); when the surface becomes wetted, the microscopic trenches fill with water, and the surface becomes more matte. Air was fully maintained on the SHPo surface (seen as completely reflective) at Re = 0, 4.69×10^6, 5.83×10^6. As Reynolds number increased, the downstream edge wetted, then de-wetted, and then the upstream edge wetted. This interesting trend has never been reported before and suggests ways to minimize wetting during high speed flows.

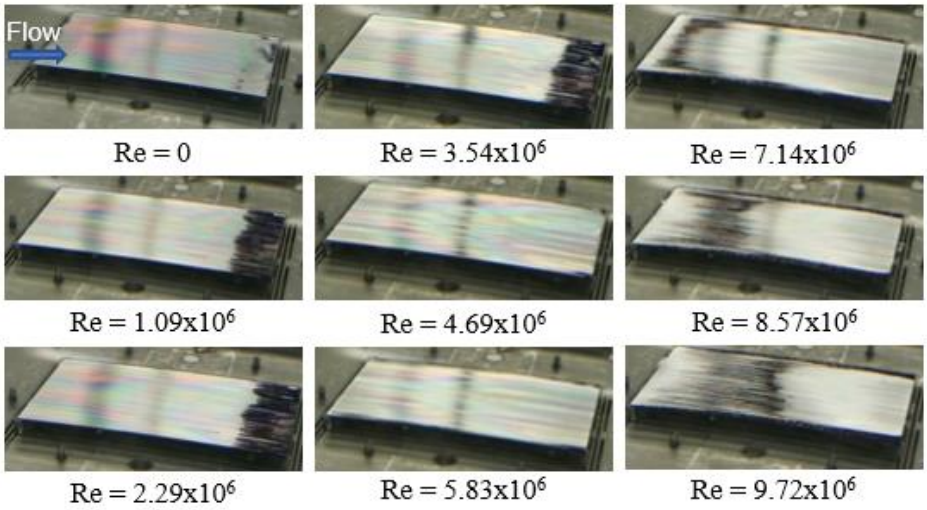

Figure 3.8: Picture sequence tracking the wetting transitions on the SHPo sample's surface. Speed is increased from Re = 0 to Re = 9.72×10^6. Silver reflective area indicates de-wetted region. Dark matte area indicates wetted region.

3.5 Post-Trip #2 Tests and Improvements for Trip #3

A test tank was built to hold window B and test for various issues identified during Trip #2 (Figure 3.9). The first issue tested was whether the displacement readings are capable of returning back to zero at the end of a test. For this test tank experiment, the samples were slightly displaced with a slow jet flow, and the displacement readings before and after the flow were both found to be about zero. The test tank experiments were unsuccessful in replicating the drastic change in start and finish displacements at zero flow seen during Trip #2, which means that the cause of the problem may have been unique to the high speed and low pressure conditions inside the tunnel.

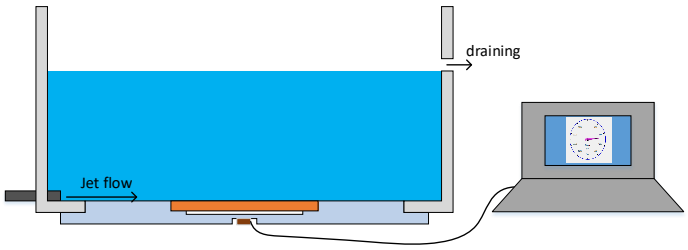

Figure 3.9: Diagram of the test tank holding window B. Jet flow from a hose will function to displace the samples for basic tests.

While testing the first issue, the samples were found to be bent. The glue screw attachment of a sample to a sample holder was found to bend the sample when tightened securely; the warped surface can potentially distort the flow boundary layer and influence the displacement data. If the sample was loosely screwed to the sample holder, the sample was less bent, but it also had a greater chance to move around during the flow experiment (Figure 3.2). This unreliable sample attachment explains how the sample could have shifted or changed in flushness during Trip #2, resulting in strange data. The glue screw method should be abandoned, and replaced with the traditional method of using one layer of strong tape to attach the sample to the sample holder.

The next problem tested was what happens to the data over a long period of time. Test tank experiments were run for lengths of time similar to a Trip #2's experiment and monitored for changes in data, but no strange shifts were seen. When the floating plate was left submerged in the test tank between runs, many bubbles were found to have accumulated underneath. The bubbles were concluded to have formed from the super-saturated water in the static test tank. The NUWC engineers provided a "Pressure versus Inlet Speed" plot (Figure 3.10) to characterize the tunnel environment during experiments. This plot reveals that a formation of bubbles could have easily occurred in the water tunnel during Trip #2, especially during the high speeds when vacuum levels are so high they increase cavitation of air in water (Figure 3.10). The presence of

bubbles may explain the displacement at the end of the Trip #2's experiment not returning back to zero, and also the SHPo sample shear stress data decreasing with increasing speed halfway through the experiment. A potential solution to bubbles interfering with sensor readings is to get rid of them once they form. Bubble formation can be monitored from underneath the transparent window (Figure 3.5); once excessive bubble accumulation is detected, the water tunnel can be stopped, partially emptied, and the floating plate can be removed so that the bubbles underneath can be blown away.

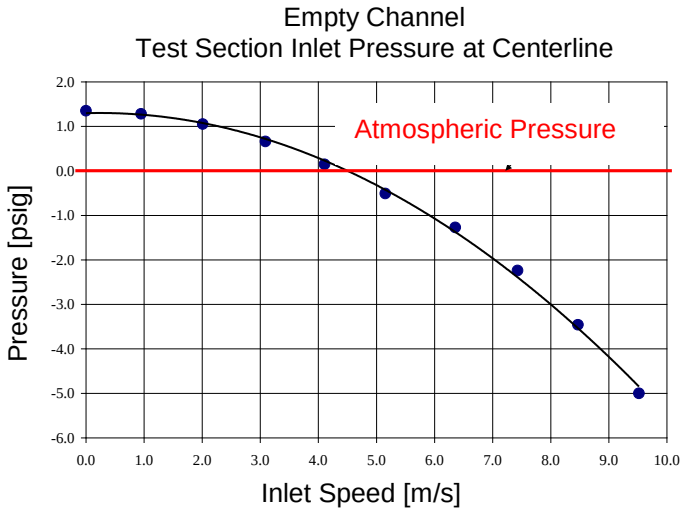

Figure 3.10: Plot of pressure versus water tunnel inlet speed, provided by NUWC. Pressure falls below atmospheric at 4.2m/s.

The last issue tested was why the software lagged during Trip #2, when the two encoders were recording at the same time. Many of the optical system's components were replaced with new ones, and the software lag was seen to decrease, but not disappear. Considering a lag still exists, a procedure modification was made to input a really large number for "Samples to

Collect" and force stop the data collection at the end of the experiment. This way data from both encoders should have enough time to be read in necessary points.

3.6 Trip #3 Experiments and Results

The setup for Trip #3 (3-day experiment) was exactly the same as the setup for Trip #2, except that the samples were no longer screwed but rather taped to the sample holders; also, window B was installed in position #3, because the usual position #2 was inaccessible due to the presence of other NUWC equipment (Figure 1.5). Next, the procedure for Trip #3 was slightly adjusted to incorporate the new information gained from the testing tank experiments. First, the software was prompted to record data until forced to manually stop, so that, even with the data collection lag, both encoders would have as much time as necessary to record a complete data set. Then, the ruler and glass slide were kept very clean of dust particles and smears, because they were found to interfere with the encoder's laser enough to cause the Interpolator's LED lights to flash red. Next, considering bubbles were found to be a big source of error during Trip #2, they were constantly monitored during Trip #3; any time an accumulation of bubbles was detected, the experiment was paused, floating plate was removed, and bubbles were blown away with a pipette.

The first experiment for Trip #3 involved collecting data for two smooth samples setup side-by-side, intending to prove that the flow conditions in the water tunnel on both sides of the window are symmetric. If the smooth surfaces are identical, flow conditions are symmetric, and the spring constants are the same, the displacements should be the equal at every speed. Even though the frame plate was initially designed to have floating plates of the same spring constant, the error in EDM fabrication and the use of the plate over time resulted in a 1.25 to 1 ratio of the spring constants. As long as the correct updated spring constant values are used to calculate shear

stress and skin friction coefficient, the data for both smooth surfaces should be very similar. The experimental skin friction coefficient data for the smooth surfaces matched one another as predicted (Figure 3.11 (a)). However, the experimental data for the smooth surfaces deviated significantly from theoretical skin friction coefficient values (Figure 3.11 (a)). This deviation from theoretical is too big to be caused by the test surface not being perfectly flush with the cover plate. The more plausible explanation is that the theoretical values may not actually be reliable or accurate. It seems that the assumption of fully developed boundary layer flow, used for theoretical calculations, is not being fulfilled during real experimental flow conditions, maybe due to disruptions in the water tunnel. Considering we cannot completely understand and quantify the flow conditions in the water tunnel, we cannot validate the assumptions necessary for theoretical value calculation and comparison. Thus, we cannot conclude whether the absolute displacement data for any surface is accurate, but we can conclude that the relative comparison of two surfaces should provide a reliable drag reduction value.

The next experiment involved collecting data for a smooth surface and a SHPo surface side-by-side, intending to measure the relative drag of one surface (SHPo) to the other (smooth) directly. During this trip, data for both surfaces was successfully collected simultaneously instead of consecutively like Trip #2, allowing for a reliable and accurate comparison of displacement data. For both surfaces, displacement increased with increase in speed, as expected. The SHPo surface showed smaller displacement values than the Smooth surface at each speed. A maximum drag reduction of 44% was seen at Re = 7.65×10^6 on the SHPo surface (Si (P50G90H50)) (Figure 3.11 (b)).

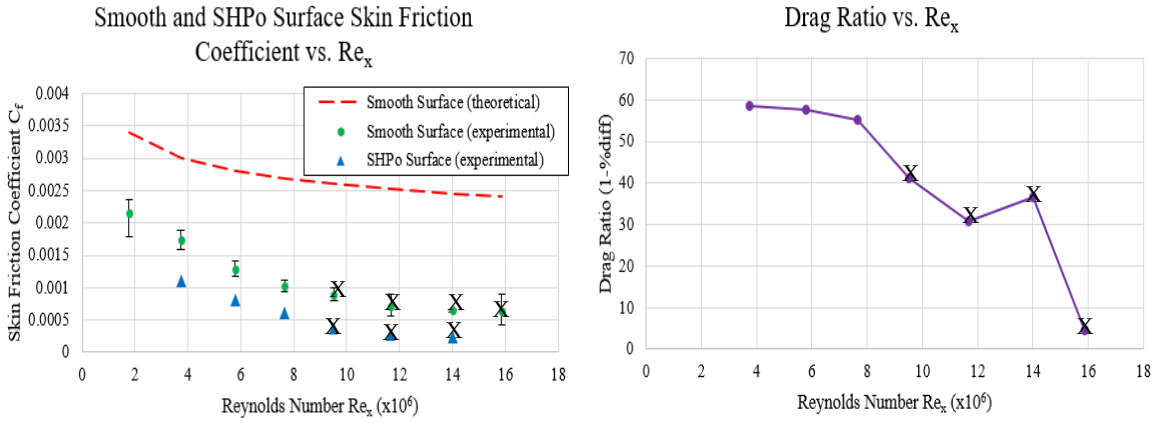

Figure 3.11: Data plots for Trip # 3. (a) Plot of shear stress versus Reynolds number, comparing experimental Smooth and SHPo surface data to theoretical Smooth data; X marks the unreliable points. (b) Plot of drag reduction versus Reynolds number; X marks the unreliable points.

While a total of eight speeds were recorded for each experiment, only five speeds were plotted to observe trends. Data past Re = 7.65×10^6 was not used because it (Figure 3.11 (a)), showed evidence of the sample surface hitting the inner edges of the cover plate (Figure 3.12). The same wall issue seen during Trip#2 was thought to be caused by the sample not being securely attached to the sample holder. However, even after the sample was better secured by replacing the glue screw method of attachment with tape, the same wall effect occurred again. The sample must be hitting the cover plate wall not because it is loose, but rather because of excessive displacement due to the large uncompensated water tunnel vibration levels. The leading edge of the sample's distance from the cover plate is set to be smaller than the trailing edge of the sample, to leave room for the drag-induced displacement along the direction of flow. However, this leading-edge distance is now found to be insufficient to compensate for the large data fluctuations in both directions at high speeds; the data was seen to reach a plateau.

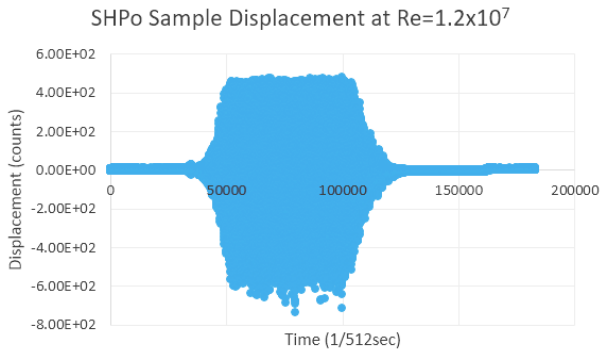

Figure 3.12: Plot of displacement versus time with a plateau. SHPo sample at Re = 1.2×10^7 was seen to hit the cover plate edge.

Next, Trip #3 data past Re = 7.65×10^6 did not return to the original displacement once the water tunnel was turned off. This same issue was seen during Trip #2 and was hoped to be solved by consistently clearing bubbles formed beneath the floating plate every 2-3 speeds. However, bubbles were seen to form very quickly during high speeds, even if the floating plate was cleared just before, proving the need for a better method for preventing bubbles. In the end, a lot more data points could be collected if the vibration and bubble issues could be solved.

3.7 Investigating Bubble Problem to Improve Trip #4

Appreciating their importance after Trip #3, we further investigated the bubble growth and prevention. A model representing the space between the bottom of a floating plate and the inside of window B was made to recreate and observe bubble growth (Figure 3.13). An aluminum block was used as the floating plate, small glass piece as the ruler, acrylic block as the window, glass slide as the cover for the encoder lens (Figure 3.13). The two blocks were held the necessary distance apart (Figure 2.3) with tape spacers. The model was placed in a cup full of water in a vacuum chamber, a two-piece plastic dome desiccator sealed with an O-ring. The

model was exposed to high vacuum and monitored for bubble growth over a long period of time. At -24kPa, approximately the same pressure as in the water tunnel during flow Re = $1.6x10^7$ bubbles formed within 10 minutes. The amount of bubbles was similar to that seen during Trip #3, yet the size was smaller probably because there was no water flow, influencing the bubbles to merge and grow. This test reassured the fact that the bubbles nucleate from super-saturated water in a high vacuum environment.

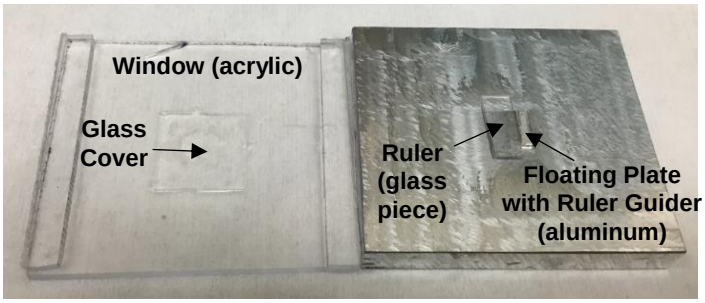

Figure 3.13: Model used for bubble tests. When the two pieces are stacked, they create a mock representation of the area between the frame plate (aluminum) and window (acrylic).

Now that bubbles can be easily created and observed, the means of prevention were investigated. Since oil has much lower air dissolution than water, it has the potential to slow down bubble nucleation in between the ruler and glass slide. A Type B microscope immersion oil made by Cargille was used for the oil, because of its high viscosity (1250 centistokes) and optically transparent qualities [10]. The previous test model (Figure 3.13) was once again used in a vacuum to test the success of the oil droplet in preventing bubble formation. After 20minutes at -24kPa, the vacuum was stopped, the model was opened up under water, and the droplet was inspected for bubbles. Since no bubbles were found, this test proved the use of oil can delay bubble formation.

Since the encoder laser must point through a uniform medium, the interface between water and oil must never pass the laser path; thus, the movement of the droplet must be tightly restricted or controlled. The contact angle of oil on glass, metal, and Teflon underwater was observed to determine the best structure to trap the oil (Figure 3.14). The oil was found to have the largest contact angle on the glass, which could thus be used as a boundary to repel the oil in a certain direction. The smallest contact angle was on the Teflon coated surface, which should be used to stick the oil in place. The bottom piece of the oil trapping structure was made up of a glass rectangular gate around a center area made of metal coated in Teflon (Figure 3.15 (a)). The top piece of the oil trapping structure was made of a glass slide with a Teflon pattered rectangle (Figure 3.15 (b)). The metal and acrylic blocks of the model used for previous tests were modified to include the oil trapping structure (Figure 3.15). Oil was place in the new model and subjected to movement similar to that experienced during experiments in the water tunnel. Even when the two model blocks were displaced slightly relative to each other or the entire model was swooshed through the water, the oil successfully stayed within its cage. Thus, the oil trapping structure modifications were successful enough to be introduced to the floating plate and window B, for hopeful bubble delay during Trip #4.

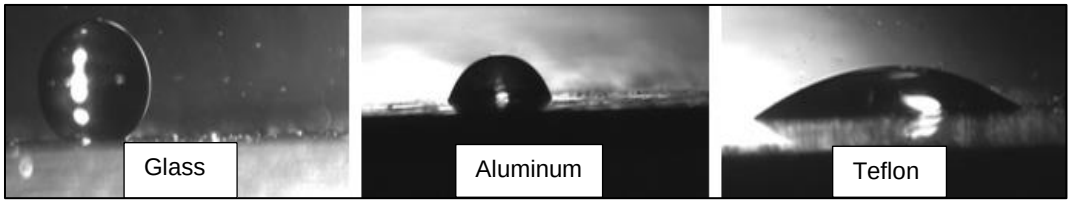

Figure 3.14: Pictures of an oil droplet on various surfaces in water, showing its contact angle.

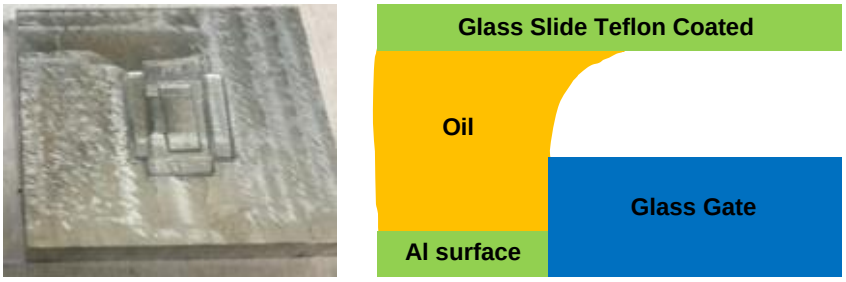

(a) (b)

Figure 3.15: Model used to test bubble formation in oil droplet. (a) Top view of the aluminum block representing the back of the floating plate; glass gate meant to hold oil droplet in place. (b) Diagram showing the resultant contact angle if oil was sandwiched between (a) and an acrylic block with a Teflon coated glass slide, representing the window.

3.8 Investigating Vibration Problem to Improve Trip #4

Vibration source and prevention was further studied after Trip #3. The water tunnel is seen to vibrate during water flow because of the compressor and pump. The shear stress sensor is directly attached to the water tunnel and thus the vibrations may be easily transmitted to the frame plate, creating large data fluctuations. The natural frequency of the floating plates was measured and compared to FFT plots for data from Trip #3. The natural frequency of the floating plates (7Hz) was found to match one the dominant peak of the FFT plots (Figure 3.16 (a)). The second peak of the FFT plots was found in the 40-50Hz range, which could be attributed to water tunnel and encoder vibration (Figure 3.16 (b)).

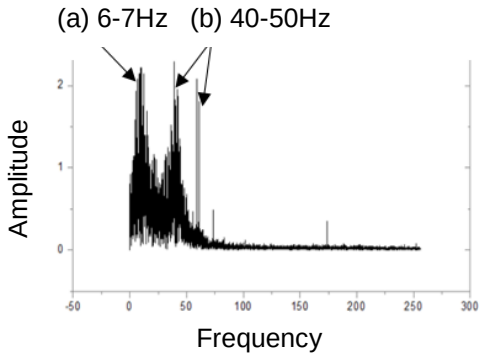

Figure 3.16: Fast Fourier Transform (FFT) of displacement data. (a) Floating plate resonance peak. (b) Water tunnel vibration peak.

The idea of using pieces of sponge between the floating plate beams for vibration dampening was tested. Many different thicknesses and arrangements of sponges were applied, the floating plate was displaced, and the displacement curve was monitored for overdamping and underdamping trends. In the end, thick pieces of sponge between each beam had the best overdamping effect (Figure 3.17 (a)), but the displacement curves did not return to zero (Figure 3.17 (b)); this is explained by the fact that the sponge may change shape plastically or shift out of position in an unpredictable manner.

Lastly, viscous oil was tested as another option for overdamping. Considering it is already being used for bubble prevention, oil could be a convenient option. The oil used would have to be changed to Type OVH, a higher viscosity (46000 centistokes) microscope immersion oil made by Cargille [10]. Also, the oil retaining structure used for bubble prevention would have to be made bigger to hold a larger volume of oil. With these modification oil was found to successfully dampen the data fluctuations and also successfully return to zero. Based on this

success, we decided to use Type OVH oil in between the floating plate and the glass slide covering the encoder.

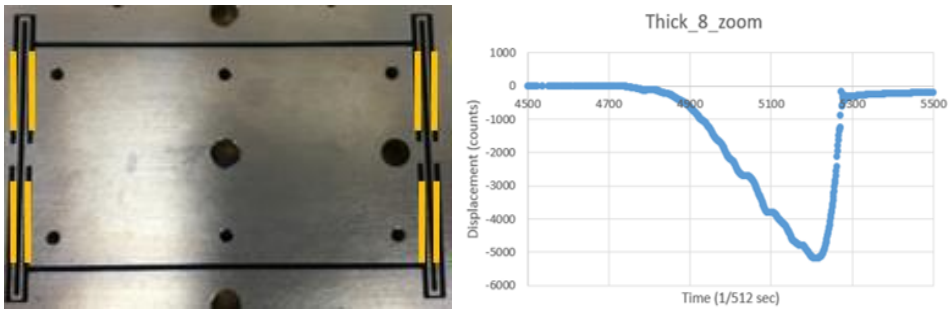

(a) (b)

Figure 3.17: Sponge test results. (a) Picture showing the placement of sponges in the floating plate's beams. (b) Plot of displacement versus time, showing signs of overdamping; however, plot does not return to zero.

3.9 Trip #4 Experiments and Results

For Trip #4 **(**1-day experiment), the same window B with the same shear stress sensor was used as for Trip #3. Yet the back of the floating plates and the inside of window B pocket was modified to incorporate the oil-retaining structures. The experimental procedure was the same, aside from the introduction of oil. Before the frame plate is placed inside the window pocket, it is flipped upside down, and oil is dripped into the gated area; then, the frame plate is submerged in the water, flipped right side up and carefully placed and attached to the window.

As expected, the oil was found to successfully minimize data fluctuations due to water tunnel vibrations. For instance, during Trip #3, the data fluctuation magnitude seen during Re = 9.6×10^6 was 500 counts, while for Trip #4 it was only 25 counts. Thus, the data was never seen to plateau. Unfortunately, however, the overdamping was seen to cause displacement instability and overall unreliable data. The displacement at each target speed did not reach stability within the

typical time frame, so the average displacement value is not valid if it still tending towards equilibrium (Figure 3.18 (a)). If the data was collected for triple the length of time, a better conclusion about displacement stability could have been made, but this would have extended the experiment for way too long to be practical.

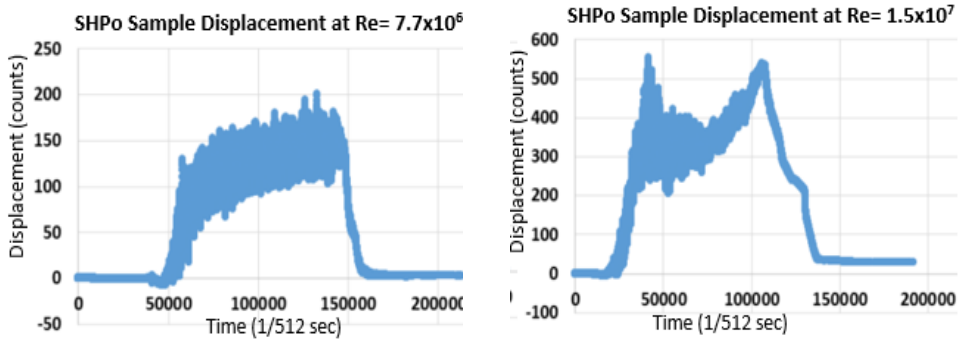

(a) (b)

Figure 3.18: Plot of displacement data for Trip #4. (a) Displacement versus time plot for Re = $7.7x10^6$; does not reach stabilization due to oil. (b) Displacement versus time plot for Re = $1.5x10^7$; warped due to bubbles.

Also, although seen to delay the formation of bubbles as expected, the oil did not prevent it completely and the improvement may be compromised by the longer stabilization time. Bubble effects were once again seen in data recorded for speeds past Re = $1.3x10^7$; the data was seen to be warped and did not return to zero (Figure 3.18 (b)). When compared to the fact that during Trip #3 bubble effects were seen much earlier on, around Re = $9.6x10^6$, the use of oil during Trip #4 allowed for the collection of a couple more data sets than before.

When compared to the complete lack of bubbles seen during the pre-testing with oil in the vacuum model, the bubble problem in Trip #4 was a surprise. Maybe no bubbles were seen

during the pre-testing, because once the vacuum was turned off, the bubbles shrank to an undetectable size. It is reasonable to assume that very viscous oil being dripped into a gated area can introduce microscopic air pockets that don't appear until high vacuum conditions expand the trapped air into a bubble. Since the vacuum model does not allow for real-time displacement measurement, bubble effects were neither numerically nor visually detected. Perhaps there are many ways bubbles can be introduced and trapped in real water tunnel experimental conditions. For example, every few speeds, the frame plate was removed to blow away any air bubbles in the vicinity of the oil droplet and check for bubbles in the oil droplet. Every time the frame plate is removed, some of the oil is stretched and separated, trapping air and water; a stick was used to remove the visible bubbles, but the microscopic impurities could not be detected.

Overall, none of the Trip #4 data was reliable and thus could not be used to calculate any drag reduction trends. Nonetheless, this trip proved that in practice oil is too messy and unpredictable to use for vibration dampening and bubble prevention.

Chapter 4 Testing Module Prototype C and Flow Experiments

4.1 Design Parameters

Distorted and shifted data from past flow experiments has shown the importance of preventing bubbles in the space between the floating plate ruler and glass slide covering the encoder lens. Bubbles are seen to form when the vacuum levels are very high, at high flow speeds in the water tunnel, because the water is super-saturated with air. In the past, the frame plate was removed from the window, between data collection periods, to clear bubbles that had formed; this was found to be ineffective at high speeds, when bubbles were found to grow within one data period (1-2minutes). Also, oil was also tried in the area between the ruler and encoder lens in hopes of decreasing the rate of bubble formation; however, the oil harmed the data even more than it helped.

The newest idea for delaying bubble formation is using under-saturated water in the area between the ruler and encoder lens. Under-saturated water can be made by boiling water to decrease the air solubility in water (mg/L) to zero. By boiling long enough to degas and cooling down quickly, the water can become highly under-saturated. A model mimicking the structure of the area between the floating plate ruler and glass slide on the encoder holder was submerged, subjected to a high vacuum similar to the water tunnel at high speeds, and the area inside the model was monitored for bubbles (Figure 4.1). No bubbles were seen after being subjected to high vacuum for an hour, so under-saturated water was successfully proved to delay bubbles. Since the space between the floating plate and the glass slide is open to the outside, the under-saturated water in the space is not contained. The best way to retain under-saturated water in the area between ruler and encoder lens is to trap it securely between the two surrounding structures.

An encoder holder was designed to screw tightly to the frame plate along the edge, while retaining a small gap in the center for holding under-saturated water. The central area between the frame plate and encoder holder unit is still open to the environment, so the surrounding super-saturated water flowing in the water tunnel diffuses in through the spaces between the floating plate beams and around the side of the sample; however, the diffusion rate through these small openings is very slow. A simple analysis predicted the water in the space would remain under-saturated throughout a full experiment with a large safety margin.

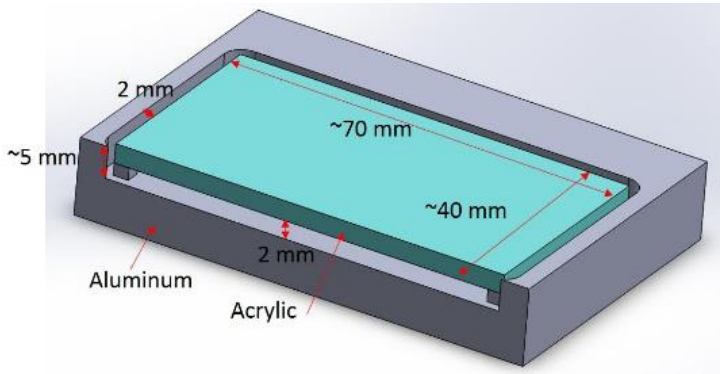

Figure 4.1: Model for trapping under-saturated water and testing for bubble growth in high vacuum.

To accommodate the encoder holder inside the window pocket, window C must be designed very similarly to window A, as shown in Figure 4.2. The window pockets will be slightly bigger than window A, because the bigger frame plate (with two floating plates) and encoder holder are used. The middle pocket does not need to be as deep as window A, because the encoder holder no longer has to be pushed up against the floating plate with a slab of rubber; instead, the newest frame plate has a sufficient number of holes to fasten both the cover plate and the encoder holder with screws. The liquid-tight cord grip and window extension are still necessary (Figure 4.2).

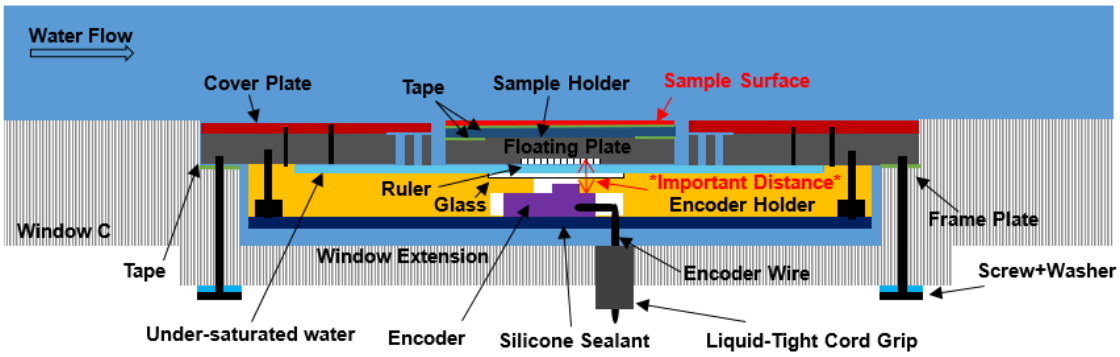

Figure 4.2: Cross-sectional schematic of window panel C.

Now that the encoders are back inside the water tunnel, water proofing of the encoder holder is of utmost priority to avoid leaks found during Trip #1. The encoder holder design is different from that used with window A and more conducive to better sealing. The encoder wires are sealed with silicone and the heads are sealed with Teflon tape (Figure 4.3). Pieces of a yellow sponge, that changes color and expands when exposed to water, were placed in the encoder holder to warn of water leakage. The sealed encoder holder underwent water-proofing tests, was first submerged in water for a full day and then was subjected to high vacuum for 30 mins while submerged in water, and passed with no signs of leakage.

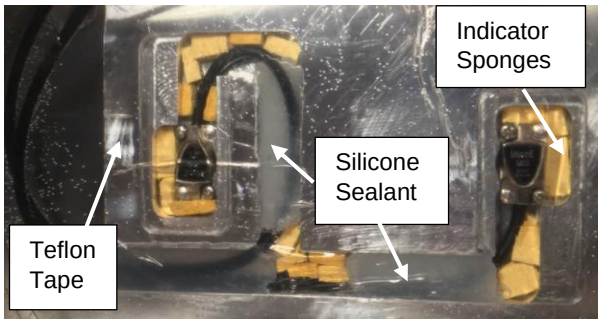

Figure 4.3: Picture of encoder holder water-proofing.

This new window C designs allows some new options for vibration dampening. In the past, oil was placed underneath the floating plates or sponges were placed in between the beams to create an over-dampening effect, but these methods were unreliable because they caused data problems, like displacement values not reaching stabilization or not returning to zero at the end of the experiment. The problems with these past attempts at vibration dampening is that they had direct interaction with the floating plates, which are very sensitive and important for correct displacement measurements. A new approach to vibration dampening targeted the frame plate, because it is the only component of the shear stress sensor that has direct contact with the vibrating window (Figure 4.2). Rubber was placed along the bottom of the frame plate to try to dampen the vibrations; however, despite trying many types and thicknesses of rubber, none were found to dampen the data fluctuations as well as the oil had during Trip #4. In the end, it was concluded that the vibration problem was left unsolved, because data can still be collected as long as the sample surface does not hit the cover plate. The new cover plate has slightly longer openings for the samples, creating leading edge gaps big enough to compensate for the large data fluctuations.

4.2 Experimental Procedure

The window C is installed in position #2 of the water tunnel. The encoder holder is placed in the window pocket, and the encoder wires are run through the two liquid-tight cord grips. A cooking pot full of under-saturated water is prepared by boiling on an induction heater (~30mins) and then cooling in a bucket of ice (~30mins). The cooled cooking pot is placed inside the water tunnel on the window C. The frame plate and encoder holder are submerged completely inside the cooking pot and a pipette is used to blow away any bubbles from the inside surfaces, the floating plate beams, and the screw holes. The two pieces are screwed together tightly in the

cooking pot, trapping under-saturated water in between (Figure 4.4). Any holes in the window are plugged with rubber stoppers, the liquid tight cord grips are tightened, and the water tunnel is filled to above the cooking pot. The water level above the cooking pot needs to be high enough to allow the pot to be tilted and the shear stress sensor to be gently removed without being exposed to air. The shear stress sensor needs to remain submerged underwater during the installation to avoid any loss of under-saturated water or introduction of air bubbles. The cooking pot is removed, the shear stress sensor is screwed onto the window, the top window is re-attached, and the water tunnel is filled to completely to prepare for flow experiments. This entire procedure has to be repeated anytime the samples need to be replacement, because under-saturated water is released (i.e., lost) when the shear stress sensor is disassembled.

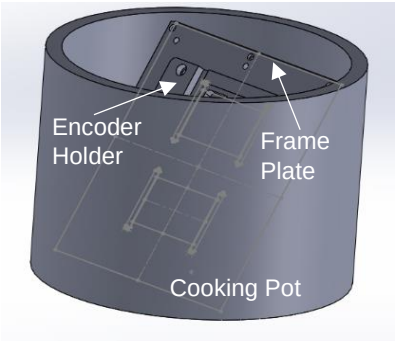

Figure 4.4: Schematic of sensor assembly in a cooking pot full of under-saturated water.

4.3 Trip #5 Experiments and Results

Right before Trip #5 (1-day experiment), a dust particle was found inside the encoder pocket near the encoder lens. To prevent the dust particle from blocking the laser and influencing the data, the Teflon tape covering the encoder head was cut out and the dust particle was removed. A new piece of Teflon tape was used to patch up the opening. Introduction of wrinkles in the patch work, was later found to be the way that water leaked into the encoder holder and malfunctioned

the encoders at the start of the Trip #5 experiment. Since there was only one functioning encoder, side-by-side data collection of the smooth versus SHPo samples was not possible. Displacement data for 8 speeds was recorded for the Smooth sample, then the Smooth sample was switched out with the SHPo sample and 8 speed data was collected for this one. Bubbles were successfully delayed as seen by the fact that data for speeds at very high vacuum levels were recorded. Also, the data showed no signs of the samples hitting a wall, proving that data fluctuations will not affect data trends as long as the leading-edge gap is large enough. The highest speed displacement data sets for the Smooth and SHPo surfaces at Re = 9.72×10^6 showed a never before seen shift in data, that could have been caused by the encoder and encoder holder physically shifting (Figure 4.5).

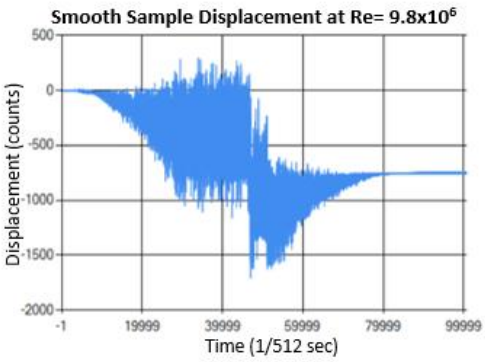

Figure 4.5: Plot showing a data shift. Plot of displacement versus time for a smooth sample at Re = 9.8×10^6, the highest flow speed so far. No data shift was seen below this speed.

The experimental smooth surface shear stress data from Trip #5 is the first data set that matched theoretical smooth data within 2.6% (Figure 4.7 (a)); it is not clear what change in this experiment, whether it be the water tunnel position, window C design or improved sample flushness, caused this successful matching. Also, data for Smooth and SHPo surfaces at all

speeds, except the highest where a shift was seen, returned to zero within 4.5counts; returning to zero is a very good indication that the shear stress sensor and window C are functioning properly. Next, the SHPo surface data showed lower shear stress values than the Smooth surface at each speed except the lowest speed (Figure 4.7 (a)). The higher shear stress value at the lowest speed could have something to do with the SHPo sample showing signs of wetting before the experiment began (Figure 4.6). The pre-wetting phenomena can be explained by the fact that the sample was submerged in under-saturated water during frame plate and encoder holder assembly in the cooking pot; SHPo surface trenches are more disposed to wetting in an environment of under-saturated water.

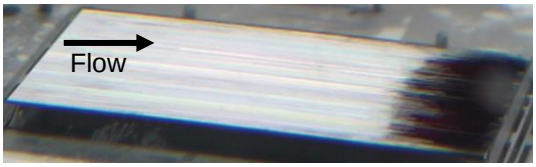

Figure 4.6: Picture of a SHPo surface pre-wetting at Re = 0. Silver color is the de-wet region. Black color is the wet region.

Lastly, data for Smooth and SHPo surfaces was collected consecutively, so the drag reduction data may be less reliable than if the data was collected simultaneously. Nonetheless, the drag reduction plot showed an expected pattern of increasing drag reduction with increasing flow speed, with a maximum drag reduction of 16.38% at Re = 5. $83x10^6$ on a SHPo surface (Si (P50G90H50)) (Figure 4.7 (b)). Overall the data from Trip #5 followed all predicted trends. Some modifications must be done for future experiment improvement, including better waterproofing and investigation into the cause of the data shift.

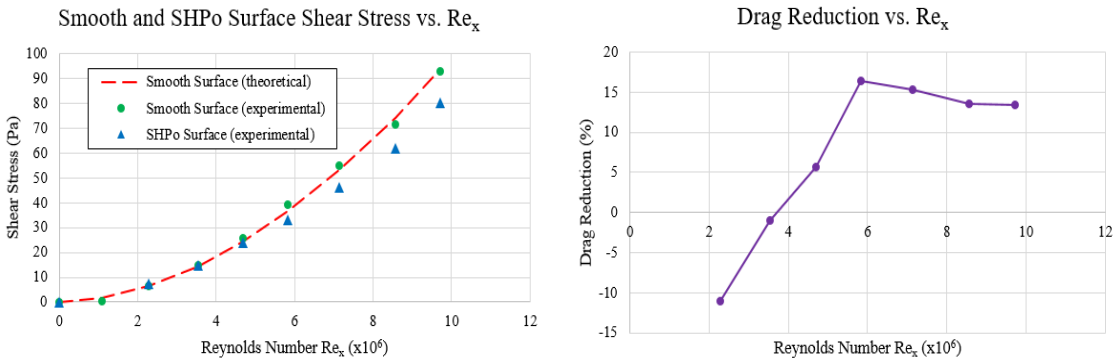

(a) (b)

Figure 4.7: Data for Trip #5. (a) Plot of smooth and SHPo surface shear stress against Reynolds number. (b) Plot of drag reduction versus Reynolds number.

4.4 Trip #6 Experiments and Results

The same window C was used for Trip #6 (1-day experiment) but some small changes were made to the shear stress system to try and solve some problems seen during Trip #5. First, the encoders were sealed completely with electronic safe silicone, not having to use any flimsy Teflon tape, to prevent water leaks damaging the encoders, as shown in Figure 4.8. Secondly, the proposed causes of the data shift were investigated; a similar data shift was reproduced when the encoder wire was pulled, jolting the encoder, and also when a bubble was forced to pass the laser. While under-saturated water greatly delays and reduces the accumulation of bubbles, the chance of a single bubble passing the laser is small but possible, and not much can be done to prevent this. Meanwhile, the other potential cause of the data shift was addressed by physically reinforcing the encoders and encoder holder with vibration resistance washers and epoxy resin.

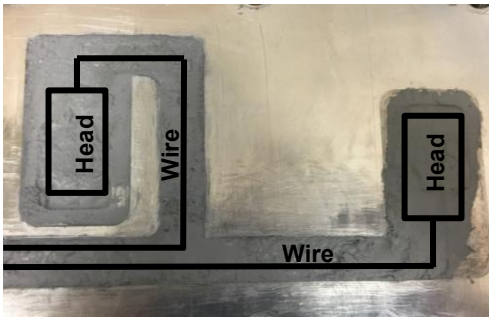

Figure 4.8: Picture of the newest water-proofing of the encoder holder. The silicone sealant covers the heads and wires of the encoders completely.

During Trip #6, the encoders were successfully sealed and did not get wet, allowing for side-by-side data recording for Smooth and SHPo surfaces. Data for the Smooth and SHPo surfaces was collected for speeds Re = 3.4×10^6 to 1.45×10^7 in increasing order and then in decreasing order. After this trial, the shear stress sensor was removed from the water tunnel, sample flushness was measured and adjusted, and the unit was reassembled with a fresh batch of under-saturated water. Then another set of data for the Smooth and SHPo surfaces was collected for the same speeds first in decreasing order and then in increasing order. The four sets of speed data were collected in different orders to check whether increasing or decreasing speed affects drag reduction data (Figure 4.9).

The first sets of data for trial 1 and 2 had overall lower drag reduction values than the second sets of data for both trials. This is suspected to be due to the SHPo sample being pre-wet by the under-saturated water when the experiment begins. The drag reduction was higher and more accurate only when the surfaces had a chance to de-wet the SHPo surface pre-wetting, which could only be done if the surface is subjected to high speeds. For trial 1, high speeds were only reached after the first set of data for increasing speed was collected, so the first five data points

were disregarded (Figure 4.9). For trial 2, high speeds were reached faster since the first set of data collected was in decreasing speed order; thus, only the first two data points were disregarded (Figure 4.9).

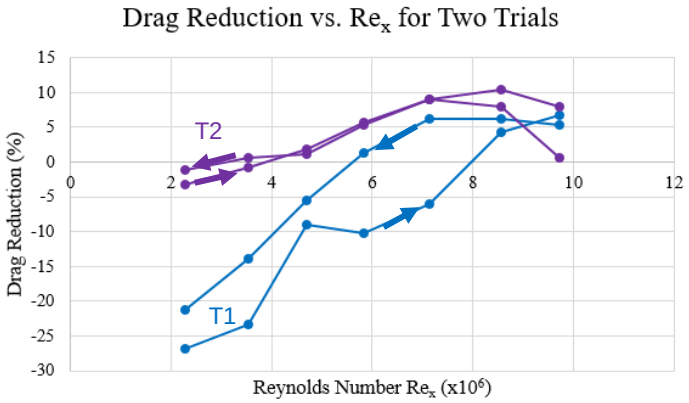

Figure 4.9: Data for Trip # 6. Plot of drag reduction versus Reynolds number for two trials. Trial one (T1) starts off with an increase in speed and then a decrease. Trial two (T2) starts off with a decrease in speed and then an increase.

When the shear stress sensor was removed to prepare for trial 2, the samples were viewed under the depth microscope for any changes in flushness with the cover plate. While the SHPo sample started out perfectly flush, after trial 1 if was found to have increased in height, causing a higher-than-expected shear stress. This change in height could have been caused by the spacers, layers of tape meant to push up the sample, dissolving and expanding underwater over time. The SHPo sample found to be protruding from the cover plate explains why the trial 1 data was seen to have negative drag reduction (shear stress for the SHPo sample was greater than the Smooth sample) for most of the experiment. Meanwhile, the trial 2 data showed reasonable positive drag reduction with a maximum of 10% seen at Re = 1.28×10^7 on a SHPo surface (Si (P50G90H50))

(Figure 4.9). These lower-than-expected drag reduction values could be attributed to sample flushness inconsistencies; thus, better spacers must be developed for more reliable sample alignment.

Lastly, data shifts were still seen during Trip #6, meaning that the physical structural reinforcements were unsuccessful and the cause is probably bubbles, which cannot be easily controlled. The data shifts are not a crippling problem, because despite a shift occurring, data can still be extracted before and after the shift (Figure 4.5). In the end, layers of tape as spacers proved to be problematic in maintaining sample flushness over the course of the experiment. Also, Trip #6 revealed the big influence pre-wetting of the SHPo surface has on drag reduction values; during the next trip, the sample pre-wetting must be de-wet before real data collection can proceed.

4.5 Trip #7 Experiments and Results

For Trip #7 (2-day experiment), the sample holders were redesigned to be more reliable. In the past, the sample holders were made of acrylic, so the threaded screw holes were more prone to thread stripping due to over-tightening and repeated use. The new sample holders were made out of aluminum, so the threaded screw holes would be stronger and could be screwed down tighter for more reliable sample flushness with the cover plate. Considering the sample holders are attached to the floating plates, the weight applied to the center platform changes the natural frequency of the floating beams. Thus, a pocket had to be machined in the aluminum sample holders to reduce the weight to that of the old acrylic sample holders, to minimize changing the floating plate frequency and potentially introducing new problems. In addition to the sample holder material, the spacer material was also changed. Previously multiple layers of various thicknesses of tape were used to raise each edge of the sample holder up enough for the sample

to be flush with the surrounding cover plate (Figure 2.4). However, too many layers of tape were problematic, because they can trap air, which can expand in high vacuum conditions, and the adhesive between each layer can dissolve over time underwater. Both of these problems contributed to unpredictable changes in spacer thickness, causing unreliable sample flushness. To avoid the problems resulting from layering tape, a new type of spacer was created. For the new spacer design, various thickness metal feeler gauges were used; to attach these feeler gauges, one layer of tape was needed, but the tape used had water-insoluble adhesive. Overall, with these design modifications, the sample holders were attached to the floating plates tightly and reliably.

Along with changes to the sample holder design, changes to the procedure were made. One change was to record data for a higher speed than ever before; the water tunnel is capable of reaching speeds up to 675RPM ($Re = 1.1x10^7$), so we wanted to take advantage of the full capabilities for a greater number of data points. Another change was made to attempt to clear the SHPo sample pre-wetting before experimental data is actually recorded. From previous data, it was seen that pre-wetting was successfully cleared after high speeds, so the new procedure was made to incorporate 5 minutes of "pre-running" the water tunnel at 600RPM ($Re = 9.7x10^6$) to try to minimize the effect of SHPo sample pre-wetting.

During the first test of Trip #7, after pre-running the water tunnel at $Re = 1.1x10^7$ for five minutes, no significant change in the SHPo sample's pre-wetting was seen. The smooth sample data for the first recorded speed of $Re = 2.3x10^6$ was irregular, in a way never before seen. Data for a few more speeds was recorded until the SHPo sample's data also became irregular; the data for both samples looked worse as the speed increased (Figure 4.10 (b)). Considering both encoders were not reading data properly, the test was stopped and the cause of the irregular data

was investigated. The shear stress sensor was removed from the water tunnel, dried, and was found to work properly in air. All the encoder components seemed to be working properly and the irregular data could not be replicated.

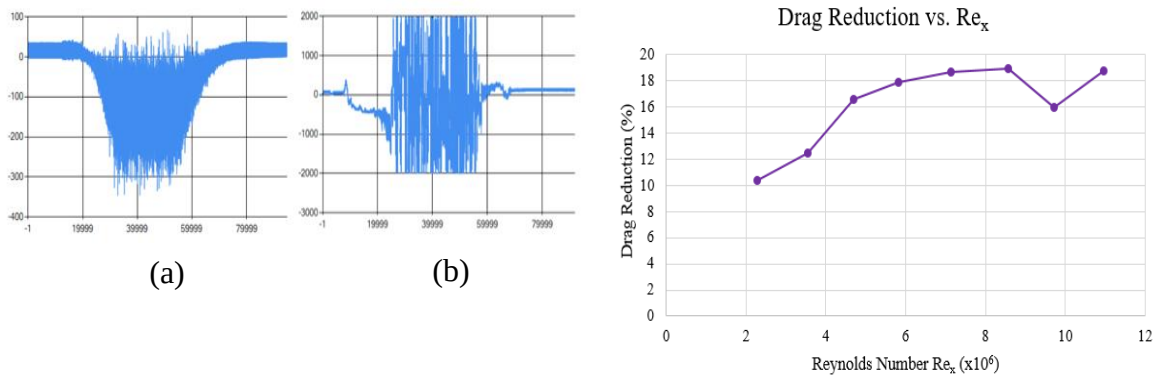

Figure 4.10: Data for Trip #7. (a) Normal displacement versus time graph seen during previous trips. (b) Abnormal displacement versus time graph seen during Trip #7. (c) Plot of drag reduction versus Reynolds number.

The shear stress sensor was reassembled in the window for another test. This time the water tunnel was pre-run at 525RPM and then 600RPM to test whether a different speed might de-wet better, but once again the pre-wetting area of the SHPo sample did not shrink. Unfortunately, this second test saw the same irregular data trends as the first test. The shear stress sensor was removed from the window and tested in a bucket underwater to see if the data behaves differently in water versus air. Once again, the encoders were found to record properly and the irregular data could not be replicated.

The next day, the tests were a little more successful in collecting displacement data for at least the first few speeds. The water tunnel was pre-run at 300RPM, seen in pictures from previous trips to de-wet the surface completely (Figure 4.6), and 600RPM, but once again this had no effect on the SHPo surface pre-wetting. Data was collected for both the Smooth and

SHPo samples simultaneously from Re = $2.3x10^6$ to $1.1x10^7$ (8 speeds) until the Smooth data became irregular. The drag reduction data showed a steady increase with increasing speed, with a maximum drag reduction value of 18.8% at Re = $1.1x10^7$ on a SHPo surface (Si (P50G90H50)) (Figure 4.10 (c)). None of the drag reduction values were negative, meaning that the sample flushness held and the sample holder design improvements were successful.

It is strange that during the previous trip, much more data was collect without any complications, than during Trip #7. The high success of Trip #6 was attributed to the efficiency of the under-saturated water in delaying bubble formation. Thus, during Trip #7, successful bubble prevention was assumed and bubbles were initially disregarded to be the cause of the irregular data plots. Nonetheless, at the end of the experiment, the sensor was disassembled underwater as a final check for bubbles; surprisingly, many small bubbles were seen between the floating plate and encoder holder (Figure 4.11), proving that bubbles were actually the cause of the irregular data. Considering the bubble problem was solved during Trip #6, but not Trip #7, something must have changed the experimental conditions significantly enough to increase the rate of bubble formation.

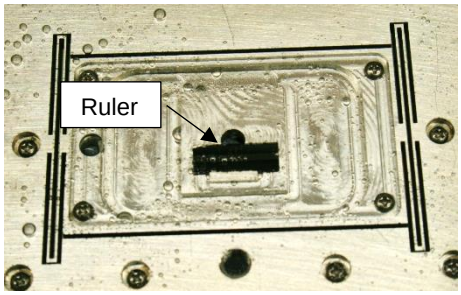

Figure 4.11: Picture of bubbles on the ruler of the floating plate.

Chapter 5 Final Flow Experiments with Various SHPo Surfaces

5.1 Improvements for Trip #8

Two changes were made for Trip #7. First, the water tunnel was pre-run at various speeds to attempt to clear the pre-wetting. However, the pre-run did not lead to any significant improvement, because it exposed the shear stress sensor to low vacuum levels faster and longer than previous tests as explained in the previous chapter. Second, the highest flow speed possible in the given water tunnel was used for the first time for Re =$1.1x10^7$ (vs. up to Re = $9.7x10^6$ in all previous trips). This highest speed exposed the shear stress sensor to vacuum levels even lower than before (-33kPa versus -23kPa). The above two procedural changes have contributed to the drastic increase in the rate of bubble formation during Trip #7 experiments despite other improvements. Accordingly, we decided to rescind the two changes for Trip #8.

Instead, for Trip #8 we used a new frame plate in window C, because the old frame plate, used for Trips #2-7, showed a drift in spring constant values over time (months). These inconsistent spring constant values could have contributed to data discrepancies, such as lower than expected or even negative drag reduction values. While the two floating plates initially had nearly identical spring constants, over time one floating plate had a 2% increase in spring constant value while the other had a 18% decrease – a significant concern. These drifts may have been due to structural corrosion and wear by being submerged for long periods of time in water, floating beams trapping dust particles, or shock impact during travel, etc. A new frame plate with new floating plates would have more consistent spring constant values and thus more reliable displacement data, leading to more accurate values of drag reduction ratio.

The new frame plate was also designed to have lighter floating plates, to increase the plate's natural frequency and thus reduce the effect of external vibrations. The sensor system could be thought of as two springs (frame plate and encoder holder) in parallel, vibrating relative to each other; when plotted as a transfer function, the sensor system was determined to act as a low-pass system. By purposefully increasing the floating plate's natural frequency (100Hz) to above the environmental noise frequency (40-50Hz), the water tunnel vibration noise would be filtered out and significantly decrease the displacement data fluctuations. Increasing the plate's resonance frequency could be the first successful solution to minimizing the vibration problem, as compared to the previous attempts to use rubber and oil for dampening.

In order to fit with the new floating plate, a new encoder holder also had to be made. Both the new floating plate and encoder holder still had the same basic dimensions, so the old cover plate, sample holders, and window C could still be used. Trip #8 was intended to quantify drag reduction for multiple types of SHPo surfaces, with different trench dimensions, in order to observe trends amongst them.

5.2 Trip #8 Experiment

For Trip #8 (4-day experiment), the first test recorded displacement trends for a smooth surface compared to another identical smooth surface. Unfortunately, after a few speeds, irregular data trends appeared, just like the ones from Trip #7. Around the same time the irregular trends began, a physical change was noticed inside of the tunnel; a significant amount of air was being sucked in through the liquid-tight cord grip and out from the side of the cover plate. At high speeds, there is always a lot of bubbles in the water, but in that moment the bubbles were more aggressive than usual. When the bottom of the transparent window was observed, the area under the encoder holder was found to be filled with bubbling water. The large influx of air from the

cord grip exposed the bottom of the encoder holder to constant movement of air bubbles, and it increased the chance of air reaching the area between floating plate ruler and encoder lens through any small opening. For instance, the screws holding the encoder holder and frame plate together had vibration resistance coils, which created small gaps easily accessible to the new abundance of super-saturated water. It is very possible that during Trip #7 and the first experiment during Trip #8 the cord grip was not tightened enough and the air influx significantly increased the rate of bubble formation to a point where the abundance of bubbles blocked the encoder and created extremely irregular data plots. To test this theory, the test module was reassembled with fresh under-saturated water, and the liquid-tight cord grip was lubricated and tightened very securely; as a result, the next test and all the rest after that were run without any bad data trends.

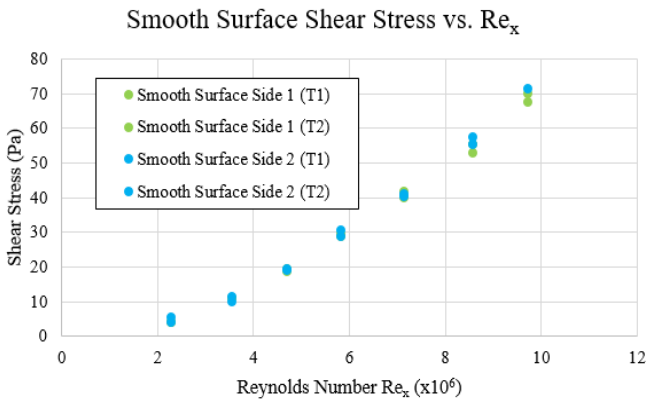

Figure 5.1: Smooth versus Smooth data. Plot of shear stress versus Reynolds number for two smooth surfaces positioned on opposite sides of the tunnel. Collected two sets of data for each smooth surface, T1 and T2.

The displacement values for the two smooth surfaces should have been identical at every speed, if the flow in the water tunnel was symmetric, the sensors were functioning, and the

surface flushness was reliable. The data for the two surfaces had a very small error and appeared quite random (Figure 5.1); thus, the flow is proven to be symmetric over the samples, and the relative drag reduction values of later tests can be expected to be reliable. Overall, the new floating plates were successful in decreasing only some of the data fluctuations due to water tunnel vibrations. The magnitude at zero flow was 5 counts as compared to 75 counts for the old plate. However, the magnitude at Re = 3.54×10^6 was 40 counts for both plates. Its seems as if making the new plate's resonance frequency higher filtered out one type of noise, present at zero flow, but did not successfully filter out another unknown noise, present during actual flow (Figure 5.2). In the end, the vibration issue may not have been completely solved, but it did not affect the data collection. The obtained data is still reliable because the cover plate was designed with enough room for the sample to move without hitting the wall at even the highest speeds and vibrations.

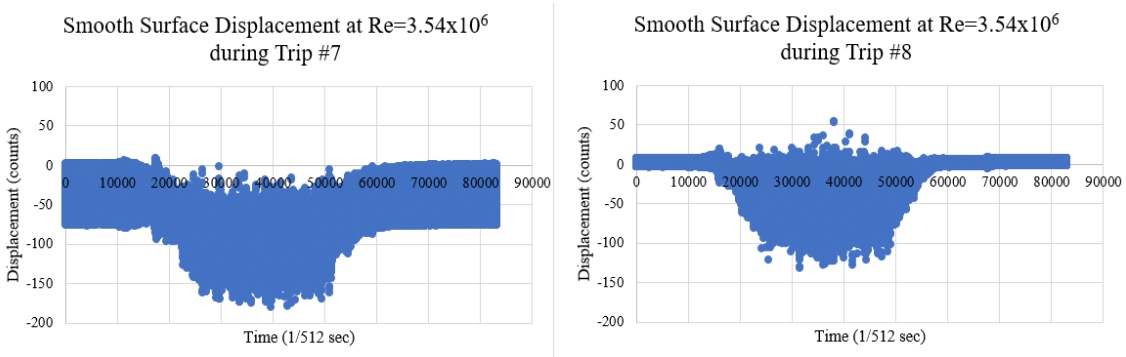

(a) (b)

Figure 5.2: Data fluctuation comparison between Trip #7 and Trip #8. (a) Displacement versus time graph for a Smooth surface at Re = 3.54×10^6 during Trip #7. (b) Displacement versus time graph for a Smooth surface at Re = 3.54×10^6 during Trip #8. The y-axes used the same scale for both graphs for better comparison.

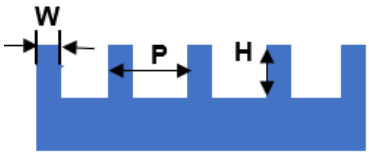

Figure 5.3: Slice view of sample surface, showing geometric parameters. P = pitch, H = height of grates, W = width of grates, G = gas fraction = (P-W)/P.

5.3 Trip #8 Results

Three sets of data at each of 8 flow speeds were collected for Si (P50G90H50) surface versus a smooth surface, Si (P25G90H30) surface versus a smooth surface, FEP (P50G90H50) surface versus a smooth surface, and Si (P50G90H30) surface versus a smooth surface. Figure 5.3 can be referenced for a better understanding of structural difference between the 4 types of SHPo surfaces. The three sets of data per speed were averaged to make drag reduction versus speed plots for each type of surface, as shown in Figure 5.4. Drag reduction values varied the most between sets at low speeds. Also, drag reduction for the lowest speed for Si (P50G90H50) and Si (P25G90H30) was negative, i.e., their drag was larger than smooth surface's. These two unreasonable data trends are specific to low speeds and can be explained by the pre-wetting phenomena seen in earlier trips; the SHPo surface is partial wetted when placed in the water tunnel by the under-saturated water in and around the plate, so the SHPo sample surface is partially wetted. Besides the first data point, the drag reduction trends are found as expected. Drag reduction steadily increases for each type of SHPo surface as the flow speed is increased. Maximum drag reduction is seen as 34.4%, 26.4%, 17.7%, 15.8%, for FEP (P50G90H50), Si (P50G90H30), Si (P50G90H50), Si (P25G90H30), respectively.

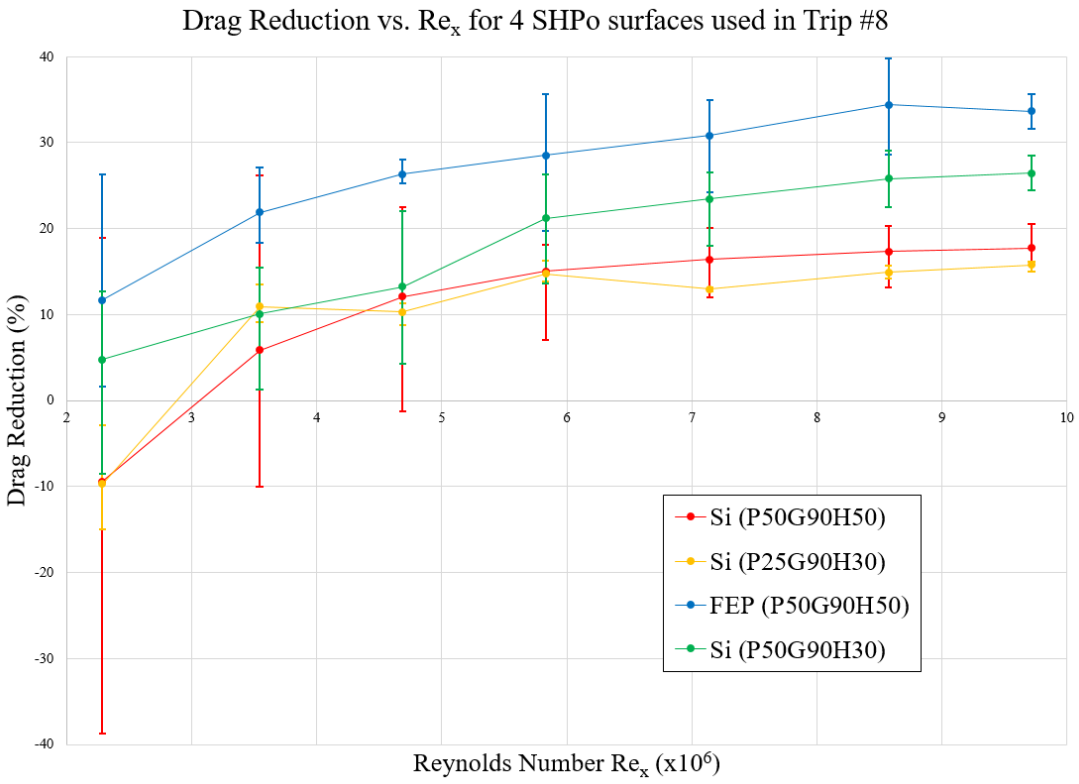

Figure 5.4: Data for Trip #8. Plot of drag reduction versus Reynolds number for four different types of SHPo surfaces. Error bars are included because multiple (3-5) trials were recorded for each type of SHPo surface.

When the drag reduction trends are plotted together for all SHPo surfaces, some conclusions can be formed about how various trench characteristics affect drag reduction. Si (P50G90H30) had a smaller trench height than Si (P50G90H50) (30 µm vs. 50 µm), and saw a larger drag reduction. Si (P50G90H30) had a larger pitch size than Si (P25G90H30) (50 µm vs. 25 µm), and saw a larger drag reduction, as shown in Figure 5.4. An increase in pitch of a SHPo surface is known to increase the slip length [11] and thus expected to increase drag reduction. A decrease in trench height may increase the duration of water-air interface at the top of the trench before sliding down into the trench [12], thus helping increase the drag reduction. However, it is

difficult to explain why the two SHPo surfaces with the same trench characteristics (P50G90H50), but one made of silicon (Si) and one made of fluorinated ethylene propylene (FEP), had such different drag reduction. Rather than speculating multiple possibilities, we decide to leave the issue to future studies. In the end, we have succeeded to obtain drag rates of multiple types of SHPo surfaces. Up to 34.4% of drag reduction has been obtained and the trend of increasing drag reduction with Reynolds number confirmed in this last experiment of the thesis project.

Chapter 6 Challenges and Limitations

6.1 Challenges

The biggest technical challenges in quantifying drag reduction on SHPo surfaces in high Reynolds number flows involved adapting our direct shear sensor to work well enough in a high vacuum and high vibration environment of the high-speed water tunnel to successfully record reliable data. Other main challenges were with the logistics of developing all the hardware parts at UCLA and carrying out the flow experiments at NUWC across the continent.

6.1.1 Vibration Problem

The water tunnel pump caused large vibrations of the water tunnel walls, which in turn vibrated the testing window and our system attached in it. These vibrations caused large data fluctuations in the displacement readings, sometimes so large that the samples attached to the floating plate hit the cover plate edge, despite a sizable gap. To better understand the source of this vibration problem, the resonance frequency of the floating plate was measured and compared with a FFT analysis of water tunnel experimental displacement data at various speeds.

To measure the resonant frequency of the floating plate, a hook was used to displace the floating plate (with sample holder and sample surface attached); upon release of the floating plate, the encoder recorded the dampening displacement curve. An FFT analysis of the dampening curve extracted a resonant frequency of 6-7Hz. Next, FFT analysis of experimental data at multiple flow speeds was completed, and signs of signal peaks below and above the resonance frequency were documented. At low speeds, two signal peaks were seen, one at a low frequency (6-7Hz) and one at a high frequency (40-50Hz); at high speeds, only the high frequency peak is seen. The first signal peak was found to match up with the previously

determined resonance frequency of the floating plate. The fact that the low frequency peak was present only at low speeds, suggests that the intensity of the other signal present might dominate the former at high speeds. The signal peak located at higher frequencies could be due to very strong environmental signals, like water tunnel vibrations.

Considering the encoder and floating plate can move relative to each other, Dr. Muchen Xu analyzed the shear stress system as a mass-spring-damper system [13]. After modeling the system as a transfer function, the shear stress sensor was determined to be a low-pass filter system. Thus, by increasing the resonance frequency of the floating plate to above the environmental noise previously detected in FFT analysis (40-50Hz), data fluctuations due to tunnel vibration could be minimized. However, the fabrication process for a new frame plate takes a long time, so meanwhile other solutions had to be tried out.

A few approaches were made to structurally modify the shear stress system to allow for vibrational damping. Sponges placed between the flexure beams suspended the floating plate and dampened the vibrations successfully, but they shifted the data, affecting the measurement accuracy. Rubber between the frame plate and window panel showed no significant damping, no matter the thickness or material. Oil underneath the floating plates successfully dampened, but highly over dampened to a point that the extended response time affected the measurement accuracy. Finally, instead of solving the vibration problem, the system was modified to prevent the huge data fluctuations from affecting data collection. The cover plate opening for the sample was made larger, so that the sample surface would not hit the cover plate edges for even the biggest data fluctuations at the highest speed. This idea was a good temporary fix, but it introduced the possibility that the larger gap between the leading edge of the sample surface and cover plate might disrupt the boundary layer of the flow over the system.

By Trip #8, the new frame plate with lighter floating plates was fabricated for higher resonance frequency. However, significant decrease in data fluctuation, compared to the old plate, was seen only at zero flow speed. The vibration problem was never completely understood or solved.

6.1.2 Bubble Problem

For the given water channel, the pressure drops to below atmospheric pressure in the test section when the flow speed increases to above 4.5m/s. The vacuum level reaches 5psig at the highest speed of 9.5m/s. This vacuum environment makes the water flowing in the test section supersaturated with air, causing air bubbles to form and grow. These bubbles would typically nucleate on a surface with many features, making the space between the frame plate and encoder holder even more vulnerable to the bubbles. The optical function of the encoder laser requires the space between the encoder lens and the displacement ruler to be clear for reliable data. Thus, the nucleation of bubbles in the laser path caused jumps and shifts in data, preventing collection of data for flow speeds past 4.5m/s.

The region between the frame plate and encoder holder was modified in hopes of delaying bubble formation. High viscosity oil in the area could ideally slow down bubble growth; however, in real experimental conditions, the application of oil is very difficult and results in trapped microscopic bubbles that were initially undetectable but expanded in vacuum conditions. Also, the use of highly viscous oil underneath the floating plates was also very messy and restricted beam displacement. Next, under-saturated water in the area was also tried as an alternative to the unreliable oil. Under-saturated water can be prepared by boiling, using a degasser, or exposing water to high vacuum, yet boiling proved to be the easiest and most convenient method. Before every experiment, under-saturated water was prepared and carefully

trapped between the frame plate and encoder holder; this method successfully slowed down bubble generation enough for data to be collected up through the highest speed of 9.5m/s, or Re = 9.72×10^6 in our tests.

6.2 Limitations

Once the water tunnel environment challenges were investigated and addressed, the shear stress and drag reduction data became more consistent and reliable. The SHPo surface's shear stress values and skin friction coefficient values were lower than the Smooth surface's, as expected. Relative drag reduction values could be determined by comparing the SHPo surface's data to the Smooth surface's data recorded simultaneously, in a water tunnel that was proven to have symmetric flow conditions. Most importantly, the drag reduction values were seen to increase as Reynolds number was increased, as predicted by some numerical studies in the literature. However, two data trends, i.e., negative drag reduction at low speeds and smooth experimental data not matching theoretical, could not be fixed or explained despite the improvements to the sensor, window panel, and test procedure. Some educated guesses as to the origin of these data trends are made in the following sections and recommendations for future investigation are made in the conclusion.

6.2.1 Negative Drag Reduction at Low Flow Speeds

Drag reduction is determined by comparing shear stress (or skin friction coefficient) data collected for a Smooth and SHPo surface at the same time under the same flow conditions. If the SHPo surface holds air in its microscale trenches, the air-water interfaces experience lower shear stress than the solid-water interfaces. As result, SHPo surfaces are expected to have lower shear stress (τ) than Smooth surfaces and experience a smaller skin friction drag:

$$Drag\ reduction = \frac{\tau_{smooth} - \tau_{SHPo}}{\tau_{smooth}}\ x\ 100 \quad (6.1)$$

A negative drag reduction means that somehow the SHPo surface was exhibiting higher drag force than the Smooth surface.

When this data trend started appearing in the earlier trips, it was attributed to the samples not being flush with the surrounding cover plate. The samples must be completely flush with the top of the cover plate to ensure no significant disruption in the turbulent boundary layer; otherwise, step up and step down features near the sample can cause abnormal displacement readings. Specifically, a sample above the cover plate will experience a higher than normal drag, and a sample below will experience a lower drag. Negative drag reduction was thought to result from the SHPo surface being significantly higher than the cover plate, and/or the Smooth surface being lower. Even though the samples were initially setup to be completely flush with the surrounding cover plate, it was later found that unreliable designs, specifically of sample attachment, sample holders, and spacers, resulted in changes of flushness during the experiment. Nonetheless, even after the designs were optimized and flushness was proven to be reliable throughout the entire experiment duration, negative drag reduction data trends were still seen.

Negative drag reduction was most often seen for the two lowest flow speeds. At these low speeds, the displacement values are very low and so the expected difference between SHPo and Smooth surface displacement is very small and easily affected by other error. For instance, human error in reading the microscope and the microscope's sensing tolerance (<0.01mm) could have resulted in detecting a slightly lower and higher alignment than reality. Also, the huge data fluctuations and encoder tolerance (0.078microns) could have limited the accuracy of low displacement readings. These errors and tolerances might have less influence on low speed data if the floating plate displacement distances would be increased, which could be done by lowering

the spring constant. Of course, however, the sensor with more flexible springs would not function for high speed flows.

Another potential source of negative drag reduction data was pre-wetting of the SHPo sample surface. After assembly in the water tunnel, but before the SHPo surface had experienced any flow, the SHPo surface already showed signs of wetting. This pre-wetting could have been due to imperfections in the silicon processing or damage to the edge of the sample; during Trips #5-8, pre-wetting could have also occurred due to exposure to under-saturated water, increasing trench susceptibility to filling. When the data for the lowest speed is recorded, the starting surface is not perfectly SHPo, because around 5-10% of the surface's trenches are already filled with water not air. This pre-wetting effect's significant influence on the loss of drag reduction values was discussed in section 4.4; in summary, a surface with pre-wetting has lower drag reduction values than the same surface that has had a chance to de-wetted a little bit, after being exposed to high speeds long enough to replenish the air in the trenches.

In the end, unless there is a way to minimize the effect pre-wetting has on drag reduction values and minimize the effect of error on small displacement values, the drag reduction data for low speeds is unreliable. The drag reduction data at these low flow speeds obtained in the experiments in this thesis lack the accuracy and need to be discarded from formal reports.

6.2.2 Experimental Data Not Matching Theoretical

Aside from Trips #5-7, Smooth experimental data was found to rarely match theoretical. At first this was thought to be caused by disruptions in boundary layer flow and the inaccuracy of the inlet position distance. Theoretical smooth surface shear stress and skin friction coefficient were calculated with the assumption of fully developed boundary layer flow and an inlet distance measured from the start of the water tunnel. However, neither of these conditions are completely

defined because flow along the bottom of the water tunnel, near the shear stress sensor, was never fully characterized. Also, steps between the water tunnel cage and windows were found to be as big as 0.02in. These steps could have disrupted the boundary layer enough to render the Equation 1.6 for calculating theoretical smooth surface shear stress invalid. When the third window test section was used, for Trips 3 and 4, the Smooth experimental data differed from theoretical even more than usual; this can be explained by the fact that placing a sample further down in the test section exposes it to more uneven areas that can disrupt the flow. One limitation of this theory is that it cannot explain why Smooth experimental data did match theoretical quite well during Trips #5-7.

Another theory was developed based on structural changes to the floating plate and encoder holder. The Smooth experimental data matched theoretical best when the floating plate and encoder holder were screwed together, providing the best assurance of x, y, z-axis tolerance for optimal encoder functioning. The data did not match when the encoders were attached to the window instead of an encoder holder. There is greater error due to machining acrylic versus aluminum, because of bending and surface finish, so the pockets in the window for the encoder could have been slightly inaccurate; misalignment in the x and y directions or incorrect spacing between ruler and encoder in the z-direction could have changed experimental data. The encoder is very sensitive to alignment, especially when being used underwater instead of in air, so any machining errors could influence displacement readings. Machining error could also explain why smooth surface experimental data did not match theoretical during the last trip, despite an aluminum encoder holder being used like Trips #5-7. For the last trip, the floating plate and encoder holder were redesigned to be lighter to increase the plate's resonance frequency, but this new design was more complicated to machine and could have also potentially introduced new

machining errors and decrease displacement reading accuracy. Overall, the machining errors seemed to be minimized for the sensor during Trips #5-7, thus this setup should be used for future experiments.

Chapter 7 Conclusion

7.1 Overview

This thesis summarizes the three testing modules prototypes (window A, window B, and window C) and eight water tunnel experiments quantifying drag reduction on SHPo surfaces. The shear stress sensor, sample holder, and testing module windows were successfully adapted for use in turbulent flows of the high-speed water tunnel at NUWC. Despite the initial challenges and limitations to the water tunnel application, the shear stress sensor was able to record consistent displacement data following predicted trends. Specifically, SHPo surfaces were found to experience lower drag than Smooth surfaces during the flow tests with Reynolds number between 4.69×10^6 and 9.72×10^6. Also, shear stresses for both surfaces increased with an increase in flow speed.

Next, drag reduction was successfully measured for all the SHPo surfaces tested in a water tunnel environment in turbulent flow conditions. The predicted trend of increasing drag reduction with increasing speed was consistently proven. The highest drag reduction value recorded for a FEP SHPo surface, with trench pitch of 50 μm, trench height of 50μm, and gas fraction of 90%, was 34.4% at $Re = 8.57 \times 10^6$. The highest drag reduction value recorded for a Si SHPo surface, with trench pitch 50μm, trench height of 30μm, and gas fraction of 90%, was 26.43% at $Re = 9.72 \times 10^6$. When comparing drag reduction data for Si (P50G90H30), Si (P50G90H50), and Si (P25G90H30), the first hints of a trend between the trench geometric parameters of SHPo surface and resulting drag reduction had emerged (Figure 5.3); specifically, a decrease in trench height or an increase in pitch size of a SHPo surface can potentially increase drag reduction.

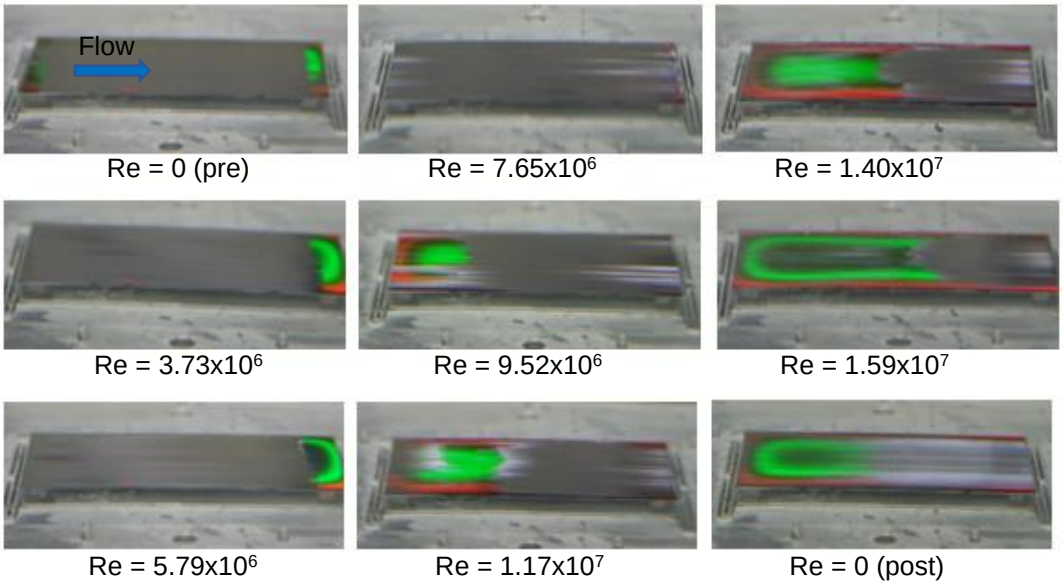

Figure 7.1: Pictures of SHPo surface's wetting dynamics over increasing flow speed from Re = 0 to Re = 1.59×10^7. They were taken during one of the experiments of Trip #3 using the SHPo surface Si (P50G90H50).

Lastly, video recordings of the SHPo surface during flow tests revealed information about wetting dynamics during turbulent, super-saturated flow in a water tunnel. One such recording from Trip #3 is shown in Figure 7.1. At low speeds, the downstream edge of the surface is wetting, but at a certain speed (Re = 7.65×10^6) the surface becomes completely de-wetted. After this de-wetting transition, the surface resumes wetting, but from the upstream edge of the surface. The physical explanation for this trend may be explained by the dynamic balance between force of the flow and force holding the air in the trenches, and also by the replenishing of air in the trenches by the surrounding super-saturated water. The super-saturated water tunnel environment, increases the stability of the air plastron [14], which explains why the SHPo surface was never completely wetted, even at Re = 1.17×10^7. Considering the SHPo surface was

seen to never completely lose the air in its trenches, there is a high possibility of some drag reduction at every speed.

7.2 Future Directions

Future work for this research would include characterization of the flow in the tunnel. Boundary layer development should be monitored throughout certain test sections, monitoring whether any water tunnel features would substantially disrupt flow along the bottom of the tunnel. This should be done to calculate the correct inlet distance and determine whether the theoretical shear stress Equation 1.6 for a smooth surface can be used in the water tunnel.

Also, further experiments could be run to determine how much changes in flushness, of the sample surface with the cover plate, may affect shear stress values. The sample's height above the cover plate can be specifically controlled to better understand past negative drag reduction trends.

Next, two different frame plates with floating plates of high and low spring constants could be used to measure high and low speed data with greater sensitivity. This could make data at low speeds more reliable and could address the previous negative drag reduction trends.

Furthermore, the influence of SHPo sample surface pre-wetting on negative drag reduction values could also be quantified by measuring the shear stress of a completely wetted SHPo surface over various speeds. Knowing the drag reduction for a SHPo surface partially wetted and the drag reduction for a SHPo surface completely wetted, one could determine the drag reduction for a SHPo surface completely de-wetted for a better understanding of the SHPo drag reduction phenomena. This type of data modification could eliminate any drag increase resulting from the SHPo surface losing its SHPo qualities with increases in flow speed.

Lastly, experiments with different types of SHPo surface should be repeated with a large enough number of samples. This could indicate more clearly how the trench pitch, trench height, or SHPo surface base material (FEP vs. Si) influence drag reduction and establish trends for a wide range of turbulent flows.

References

[1] Park, Hyungmin, Guangyi Sun, and Chang-Jin Kim. "Turbulent Drag Reduction on Superhydrophobic Surfaces Confirmed by Built-in Shear Sensing." *IEEE International Conference on Micro Electro Mechanical Systems (MEMS)* 26 (2013): 1183-186.

[2] Lee, Choongyeop, Chang-Hwan Choi, and Chang-Jin Kim. "Structured Surfaces for a Giant Liquid Slip." *Physical Review Letters* 101.6 (2008).

[3] Sun, Guangyi, Hyungmin Park, and Chang-Jin Kim. "Development of a Miniature Shear Sensor for Direct Comparison of Skin-Friction Drags." *Journal of Microelectromechanical Systems* 24.5 (2015): 1426-435.

[4] Park, Hyungmin, Guangyi Sun, and Chang-Jin Kim. "Superhydrophobic Turbulent Drag Reduction as a Function of Surface Grating Parameters." *Journal of Fluid Mechanics* 747 (2014): 722-34.

[5] "Tape & Glass Scales." *Celera Motion*. <http://www.celeramotion.com/products-services/tape-glass-scales/portfolio-page>.

[6] "Mercury M1000 Analog Output Linear Kit Encoder." *Celera Motion*. <http://www.celeramotion.com/products-services/linear-encoders-compact/m1000>.

[7] "QSB Quadrature to USB Adapter." *US Digital*. <http://www.usdigital.com/products/interfaces/pc/usb/QSB>.

[8] Lauga, Eric, and Howard A. Stone. "Effective Slip in Pressure-driven Stokes Flow." *Journal of Fluid Mechanics* 489 (2003): 55-77.

[9] Maclean, Matthew, and Joseph A. Schetz. "Numerical Study of Detailed Flow Affecting a Direct Measuring Skin-Friction Gauge." *AIAA Journal* 41.7 (2003): 1271-281.

[10] "Immersion Oil and the Microscope." *Cargille Labs*. <http://www.cargille.com/immersionoilmicroscope.shtml>.

[11] Lee, Choongyeop, Chang-Hwan Choi, and Chang-Jin Kim. "Structured Surfaces for a Giant Liquid Slip." *Physical Review Letters* 101.6 (2008).

[12] Xu, Muchen, Guangyi Sun, and Chang-Jin Kim. "Infinite Lifetime of Underwater Superhydrophobic States." *Physical Review Letters* 113.13 (2014).

[13] Xu, Muchen. *Design, Fabrication, and Evaluation of Superhydrophobic (SHPo) Surfaces for Drag Reduction in Turbulent Boundary Layer Flows.* Ph.D. dissertation, UCLA, Los Angeles, CA, 2017.

[14] Xu, Muchen, Guangyi Sun, and Chang-Jin Kim. "Wetting Dynamics Study of Underwater Superhydrophobic Surfaces through Direct Meniscus Visualization." *IEEE International Conference on Micro Electro Mechanical Systems (MEMS)* 27 (2014): 668-71.